A&A 381, 571–605 (2002)
DOI: 10.1051/0004-6361:20011516

Astronomy & Astrophysics

ISO spectroscopy of compact H II regions in the Galaxy

I. The catalogue⋆

E. Peeters[1,2], N. L. Martín-Hernández[2], F. Damour[3], P. Cox[4], P. R. Roelfsema[1], J.-P. Baluteau[3], A. G. G. M. Tielens[1,2], E. Churchwell[5], M. F. Kessler[6], J. S. Mathis[5], C. Morisset[3], and D. Schaerer[7]

[1] SRON-Groningen, PO Box 800, 9700 AV Groningen, The Netherlands
[2] Kapteyn Institute, PO Box 800, 9700 AV Groningen, The Netherlands
[3] Laboratoire d'Astrophysique de Marseille, CNRS & Univ. de Provence, BP 8, 13376 Marseille Cedex 12, France
[4] Institut d'Astrophysique Spatiale, Bât. 121, Université de Paris XI, 91405 Orsay, France
[5] Department of Astronomy, 475 North Charter Street, University of Wisconsin, Madison, WI 53706, USA
[6] ISO Data Centre, Astrophysics Division, ESA, Villafranca, Spain
[7] Laboratoire d'Astrophysique, Observatoire Midi-Pyrénées, 14, Av. E. Belin, 31400 Toulouse, France

Received 3 August 2001 / Accepted 19 October 2001

Abstract. Infrared spectra between 2.3 and 196 μm were taken towards a sample of 45 compact H II regions using the two spectrometers (SWS and LWS) on board ISO. The primary goal is to determine the distribution of element abundances in the Galaxy, although there are also many other uses of this database. The spectra contain a wealth of information on the ionized gas and the associated photodissociation regions through the atomic fine-structure lines and on the dust properties via the dust emission bands and the continuum. Significant variations are found from source to source in both spectral shape and content. The sample of H II regions spans a wide range in galactocentric distance (from 0 to 22 kpc) enabling to investigate the variations of the nebular properties across the Galactic plane. The observations and the data reduction are described in detail in the present paper. The ISO spectral catalogue of compact H II regions contains the combined SWS-LWS spectra for each of the sources, the fluxes of the atomic fine-structure lines and hydrogen recombination lines, and an inventory of the spectra in terms of molecular lines, dust and ice bands.

Key words. catalogues – H II regions – Galaxy: abundances – infrared: ISM: lines and bands – infrared: ISM: continuum

1. Introduction

H II regions are photoionized regions surrounding OB stars. When the O and B stars are newly formed, they are still deeply embedded in their parental molecular cloud and the associated regions of ionized gas are generally small (with linear sizes below ∼0.1 pc) and dense ($n_e \geq 10^4$ cm^{-3}). These "ultracompact" H II regions evolve further into "compact" H II regions when the dense, ionized gas grows in size at the expense of the molecular gas (e.g., Churchwell 1990; Garay & Lizano 1999). Ultracompact H II regions are known to be the most luminous objects in the Galaxy at far-infrared wavelengths (Churchwell 1990) and the dust in and around these regions absorbs most of the stellar luminosity which is then re-emitted in the infrared. Due to the high degree of obscuration, most ultracompact and compact H II regions can only be studied at radio and infrared wavelengths. Whereas many radio studies are available (e.g., Wood & Churchwell 1989; Kurtz et al. 1994; Afflerbach et al. 1996; Kurtz et al. 1999), observations for large samples of ultracompact and compact H II regions in the infrared have been done at either low spatial resolution or with poor resolving powers using the IRAS LRS data (e.g., Simpson & Rubin 1990) or ground-based observations (Faison et al. 1998). Observations of selected atomic fine-structure lines were made with the Kuiper Airborne Observatory (KAO) for ∼40 compact H II regions (Simpson et al. 1995; Afflerbach et al. 1997; Rudolph et al. 1997, and references therein).

Send offprint requests to: E. Peeters,
e-mail: peeters@astro.rug.nl

⋆ Based on observations with ISO, an ESA project with instruments funded by ESA Member States (especially the PI countries: France, Germany, The Netherlands and the UK) and with the participation of ISAS and NASA.

Finally, detailed studies have been made from the ground towards a few sources (e.g., Roelfsema et al. 1989; Watarai et al. 1998; Feldt et al. 1999; Takahashi et al. 2000).

The two spectrometers on board the Infrared Space Observatory (ISO, Kessler et al. 1996), the Short Wavelength Spectrometer (SWS, de Graauw et al. 1996) and the Long Wavelength Spectrometer (LWS, Clegg et al. 1996), provided a unique opportunity to measure spectra from 2.5 to 196 μm with resolving powers $\frac{\lambda}{\Delta\lambda}$ between 150 and 500, towards 45 Galactic H II regions. The spectral coverage gives access to nearly all the atomic fine-structure and hydrogen recombination lines in the infrared range. In addition to the atomic emission lines, the ISO spectra reveal the shape of the strong dust continuum and several emission features. Absorption bands from molecular ice species were detected toward some sources. The observed H II regions were carefully selected to sample the Galactic disk out to 22 kpc from the center, permitting a study of Galactic abundance variations over a larger range than in previous studies. The information contained in the combined SWS-LWS grating spectra provides a basis for a broad range of studies including the properties of H II regions, the characteristics of associated dust and the abundance gradients in the Galaxy.

This Paper presents for each source the combined SWS-LWS spectrum, the measured line fluxes for all the atomic emission lines and the inventory of the detected molecular lines and the dust and ice bands. An accompanying Paper (Martín-Hernández et al. 2002, hereafter Paper II) will discuss the first results of the properties of the compact H II regions and the element abundance as derived from the present data.

The sample of compact H II regions with their observations are discussed in Sect. 2. Section 3 gives a detailed description of the reduction of the SWS and LWS data; the line flux determination, the error determination and the influence of the source structure on the observed fluxes are discussed in Sect. 4. Section 5 compares the ISO data with corresponding KAO and IRAS observations. Characteristics of the H II regions such as the kinematical distance, the luminosity and the morphology are described in Sect. 6. The ISO spectra, the line fluxes, the detected molecular lines and dust and ice bands are presented and discussed in Sect. 7 for each H II region of the sample. This section contains the core of the paper. A summary is given in Sect. 8.

2. Observations

In the "Ultracompact H II Region" (UCH II) ISO program, a total of 45 H II regions were observed using the SWS and the LWS in the grating mode yielding complete spectra from 2.3 to 196 μm. The data were obtained with two guaranteed time programs (ISM_IV01 and ISM_IV02) as well as a solicited proposal (ZZ_ISM).

2.1. The sample

The H II regions were selected primarily to be observable with the SWS and the LWS. First, the sources were required to be bright enough (at least a few Jy in the IRAS 12 μm band) to ensure detectability with both instruments. Second, the nebulae had to be compact with sizes smaller than the SWS and LWS beams (i.e. $\lesssim 20''$) so that all the nebular flux is within both beams. Six sources are point-like for the ISO spectrometers, i.e. with mid-infrared sizes $\leq 5''$. Third, to minimize confusion problems, isolated regions were prefered over sources lying in complexes. Finally, the sources were chosen to cover as wide a distribution as possible in galactocentric distance in order to derive the Galactic element abundance over larger scales than in previous studies. ISO was pointed at the IRAS positions of the selected IRAS sources. The sample was enlarged by DR 21 and Sgr C.

For two of the sources, IRAS 18316−0602 (also known as GL7009) and IRAS 19110+1045, the 2.3 to 196 μm spectra were found to be dominated by absorption and they are not considered in this catalogue. A detailed analysis of their spectral content can be found in Dartois et al. (1998). The sample considered for this catalogue consists therefore of 43 H II regions which are listed in Table 1. For each source, the name, the equatorial coordinates of the position observed with the SWS and LWS, the date of the observation, the Target Dedicated Time (TDT) of the observations (which uniquely identifies each observation) and some other common designations are given in Table 1. For the majority of the sources, the SWS and LWS observations were concatenated, i.e. the LWS spectrum was measured immediately after the SWS observation was completed. For Sgr C, only an SWS spectrum was taken in the UCH II ISO program and the LWS full grating spectrum was extracted from the ISO archive.

2.2. The SWS observations

The SWS grating spectra were taken in the so-called Astronomical Observation Templates 01 (AOT 01) full scan mode (de Graauw et al. 1996) speed 2. The SWS has two spectrometer sections: the short wavelength section (SW) covering 2.3 to 12 μm, and the long wavelength section (LW), from 11 to 45 μm, yielding a total wavelength coverage of 2.3–45 μm. The combined spectrometer sections are composed of 12 separate grating bands, the AOT bands (see Table 2). Each AOT band is defined through a combination of detector array (1×12 detectors), instrument aperture and grating order. The SWS has three apertures with sizes of $14'' \times 20''$ for bands 1 and 2, of $14'' \times 27''$ for bands 3A, 3C and 3D, of $20'' \times 27''$ for band 3E and of $20'' \times 33''$ for band 4.

In the AOT 01 mode, spectra are taken by scanning the grating over its full mobility range and back. Thus, for each detector of a detector array and each AOT band two independent scans are obtained; one "up" and one "down" scan. As a result, 24 independent measurements of the

Table 1. Journal of observations. The coordinates of the positions observed with ISO are given.

Source	RA (J2000.0)	Dec (J2000.0)	Date	TDT$^{\diamond}$ SWS	TDT$^{\diamond}$ LWS	Galactic name	Other designations
IRAS 01045+6506	01 07 50.7	+65 21 21.7	18-Mar.-98	85303602	-	G124.64+2.54	WB 380
IRAS 01420+6401	01 45 39.6	+64 16 02.1	21-Jul.-97	61301076	61301075	G128.77+2.01	WB 399
IRAS 02219+6125	02 25 44.6	+62 06 11.3	23-Aug.-97	64600609	-	G133.70+1.20	W3 A, RAFGL 326
			11-Jan.-98	78800709	78800710		
IRAS 02383+6241	02 42 19.8	+62 53 51.8	3-Mar.-98	83901404	83901403	G135.18+2.69	WB 436
IRAS 02575+6017	03 01 31.3	+60 29 13.5	27-Mar.-98	86300968	86300969	G138.29+1.55	WB 463, RAFGL 4029
IRAS 04025+5313	04 06 25.5	+53 21 50.0	26-Sep.-97	68100312	68100305	G149.59+0.90	WB 529
IRAS 05167+3858	05 20 11.1	+39 01 19.7	22-Aug.-97	64501216	64501206	G168.68+1.08	WB 625
IRAS 05221+4139	05 25 39.8	+41 41 50.3	22-Aug.-97	64501104	64501107	G167.06+3.46	WB 640
IRAS 05302+3739	05 33 40.1	+37 41 07.3	22-Aug.-97	-	64501371	G171.26+2.54	WB 656
IRAS 05335+3609	05 36 52.6	+36 11 00.3	8-Oct.-97	-	69201373	G172.87+2.26	WB 668
IRAS 06158+1517	06 18 44.8	+15 16 43.4	13-Mar.-98	84901804	84901903	G195.65−0.10	Sh 266, WB 794
IRAS 10589−6034	11 00 59.8	−60 50 27.1	11-Aug.-96	26800760	26800723	G289.88−0.79	RAFGL 4122
IRAS 11143−6113	11 16 33.8	−61 29 59.4	5-Aug.-96	26200509	26200510	G291.86−0.68	RAFGL 4127
IRAS 12063−6259	12 09 01.1	−63 15 54.7	2-Aug.-96	25901414	60900713	G298.19−0.78	RAFGL 4144
IRAS 12073−6233	12 10 00.3	−62 49 56.5	2-Aug.-96	25901572	25901573	G298.23−0.33	
IRAS 12331−6134	12 36 01.9	−61 51 03.9	10-Sep.-96	29900470	29900475	G301.11+0.97	
IRAS 15384−5348	15 42 17.1	−53 58 31.5	10-Sep.-96	29900661	29900628	G326.44+0.91	
IRAS 15502−5302	15 54 06.0	−53 11 36.4	5-Aug.-97	27301117	62802718	G328.31+0.43	
IRAS 16128−5109	16 16 39.3	−51 16 58.3	6-Sep.-96	29402233	29402234	G332.15−0.45	
IRAS 17160−3707	17 19 26.1	−37 10 53.8	6-Oct.-96	32400821	32400822	G350.10+0.09	
IRAS 17221−3619	17 25 31.7	−36 21 53.5	12-Oct.-96	33100380	33100376	G351.46−0.44	
IRAS 17279−3350	17 31 18.0	−33 52 49.4	3-Oct.-96	32200877	32200878	G354.20−0.05	RAFGL 5347
Sgr C	17 44 35.6	−29 27 29.3	5-Mar.-98	84100301	-	G359.43−0.08	
	17 44 35.9	−29 27 54.3	11-Mar.-98	-	84700220		
IRAS 17455−2800	17 48 41.5	−28 01 38.3	29-Aug.-96	28701327	28701328	G1.13−0.11	Sgr D
IRAS 17591−2228	18 02 13.2	−22 27 58.9	14-Apr.-97	51500580	51500579	G7.47+0.06	
IRAS 18032−2032	18 06 13.9	−20 31 43.2	14-Apr.-97	51500478	51500477	G9.61+0.20B	RAFGL 5436
IRAS 18116−1646	18 14 35.2	−16 45 20.6	13-Apr.-96	14801733	14801732	G13.88+0.28	
IRAS 18162−2048	18 19 12.0	−20 47 31.1	13-Apr.-96	14802136	14802135	G10.84−2.59	RAFGL 2121
IRAS 18317−0757	18 34 24.9	−07 54 47.9	8-Mar.-97	47801040	47801041	G23.96+0.15	RAFGL 2194
IRAS 18434−0242	18 46 04.0	−02 39 20.5	17-Apr.-96	15201383	15201381	G29.96−0.02	RAFGL 2245
IRAS 18469−0132	18 49 33.0	−01 29 03.7	26-Oct.-97	71100888	71100887	G31.40−0.26	
IRAS 18479−0005	18 50 30.8	−00 01 59.4	17-Apr.-96	15201791	15201792	G32.80+0.19	RAFGL 5536
IRAS 18502+0051	18 52 50.2	+00 55 27.6	17-Apr.-96	15201645	15201645	G33.91+0.11	RAFGL 5541
IRAS 19207+1410	19 23 02.4	+14 16 40.6	15-Apr.-96	15001041	15001039	G49.20−0.35	RAFGL 2379
IRAS 19442+2427	19 46 20.1	+24 35 29.4	15-Apr.-96	15000444	15000443	G60.90−0.10	RAFGL 2454, Sh 87
IRAS 19598+3324	20 01 45.6	+33 32 43.7	11-Apr.-96	14601350	14601348	G70.29+1.60	K3-50 A
			4-Dec.-96	38402466	-		
DR 21	20 39 00.9	+42 19 41.9	17-Apr.-96	15200555	15200786	G81.70+0.54	RAFGL 2624
IRAS 21190+5140	21 20 44.9	+51 53 26.5	24-Apr.-96	15901853	15901854	G93.53+1.47	M1-78
IRAS 21270+5423	21 28 41.9	+54 36 51.5	13-Feb.-98	82100309	82100310	G96.29+2.59	Sh 127A, WB 85A
IRAS 21306+5540	21 32 11.4	+55 53 23.9	15-Feb.-98	82301012	82301011	G97.52+3.18	Sh 128, WB 91
IRAS 22308+5812	22 32 45.9	+58 28 21.0	12-May-96	17701258	17701257	G105.63−0.34	Sh 138, WB 191
			30-May-97	56101082	56101081		
IRAS 23030+5958	23 05 10.6	+60 14 40.6	24-Jun.-96	22000961	22000962	G110.10+0.05	Sh 156, WB 240
IRAS 23133+6050	23 15 31.4	+61 07 08.5	24-Jun.-96	22001506	22001505	G111.62+0.37	Sh 159, WB 261

NOTE. Units of right ascension are hours, minutes, and seconds, and units of declination are degrees, arcmin, and arcsec.
$^{\diamond}$ Target dedicated time (TDT) which uniquely identifies each observation.

incident spectrum are obtained (i.e. 2 scans × 12 detectors). Due to the sampling strategy of the SWS AOT 01 mode, each of these independent measurements individually is under-sampled. However, because the measurements are obtained at slightly different wavelength offsets they can be combined to yield a factor of four oversampled spectrum. The spectrum nominally has a spectral resolving power of $\frac{\lambda}{\Delta\lambda} \sim 450$ and a wavelength accuracy of about 10% of a resolution element. By comparing the independently reduced up and down scans for a given source, an estimate of the instrumental uncertainty can be obtained.

Table 2. The SWS AOT bands and LWS detectors.

SWS			LWS	
Band	λ^* (μm)	$1\sigma^\diamond$ (%)	Detector	λ^* (μm)
1A	2.38–2.61	4	SW 1	43.0–50.5
1B	2.60–3.03	4	SW 2	49.5–64.0
1D	3.02–3.53	4	SW 3	57.0–70.0
1E	3.52–4.06	4	SW 4	67.0–82.0
2A	4.05–5.31	8	SW 5	76.0–93.0
2B	5.30–7.01	8	LW 1	84.0–110.0
2C	7.00–12.1	8	LW 2	103.0–128.0
3A	12.0–16.6	16	LW 3	123.0–152.0
3C	16.5–19.6	16	LW 4	142.0–171.0
3D	19.5–27.6	16	LW 5	161.0–196.0
3E	27.5–29.0	23		
4	28.9–45.2	25		

* Official band ranges. $^\diamond$ 1σ absolute flux accuracy (R. Shipman, private communication). SW = short-wavelength section, LW = long-wavelength section.

For calibration purposes, the compact H II region K3-50 A has also been observed with the SWS in the AOT 01 mode speed 4 yielding a spectral resolving power of $\simeq$1600. The results on K3-50 A reported in the catalogue refer to the AOT 01 mode speed 4 data (TDT = 38402466).

2.3. The LWS observations

The LWS spectra were measured using the LWS AOT 01 mode (Clegg et al. 1996). The LWS has two spectrometer sections: the short wavelength section (SW) covering 43 to 93 μm, and the long wavelength section (LW), from 84 to 196 μm, yielding a total wavelength coverage of 43–196 μm. Each spectrum consists of ten overlapping subspectra, one for each of the ten detectors. The LWS field of view is restricted by an internal field mirror to provide an approximately circular footprint on the sky with a wavelength dependent diameter of $\sim$80″ (for the exact diameter see the ISO Handbook volume IV: "LWS – The Long Wavelength Spectrometer" by Gry et al. 2000). The official wavelength ranges are given in Table 2 for the ten LWS detectors.

In the AOT 01 mode, spectra are taken by scanning the grating 3 times over its full mobility range and back. For each target, 6 scans are obtained, 3 in "up" and 3 in "down" direction. Combined these scans yield a spectrum sampled at 1/4 of a spectral resolution element. The resolution element is 0.283 μm for detectors SW1–SW5 (43–93 μm) in second spectral order and for detectors LW1–LW5 (84–196 μm) in first order, it is 0.584 μm. The resolving power, $\frac{\lambda}{\Delta\lambda}$, of the LWS grating spectra varies from 140 to 330. Analoguous to SWS, an estimate of the instrumental uncertainty can be obtained by comparing the independently reduced up and down scans for a given source.

3. Data reduction

One of the aims of this study is to derive line ratios across the available wavelength range and to combine the spectra measured by the SWS and the LWS. This requires a detailed understanding of the calibration between: i) the two spectrometers, ii) the different bands of the SWS, and iii) the different detectors of the LWS. This knowledge will define the limits of the present dataset and constrain any conclusion one can draw from the line fluxes given in the tables of this catalogue.

The following gives a detailed account of the reduction of both the SWS and the LWS data. Since the SWS reduction requires more steps than the LWS reduction and since new methods were applied, we describe in more detail the SWS data reduction.

3.1. SWS data reduction

The SWS data were processed with IA^3, the SWS Interactive Analysis package (de Graauw et al. 1996) using calibration files and procedures applied in the IA^3 test version of Aug. 4, 2000 (except for the flux calibration files, see Sect. 3.1.1), corresponding to a stable test-phase of OLP10 (Off-Line Processing 10).

For a general description of the SWS instrument and its reduction, we refer to the ISO Handbook volume VI: "SWS – The Short Wavelength Spectrometer" by Leech et al. (2001). The standard reduction process consist of corrections for the electronics of the system, dark current subtraction, correction for the relative spectral response of the instrument (RSRF) and wavelength and flux calibration. Finally, the wavelengths are corrected for the ISO velocity resulting in an Auto Analysis Result (AAR).

In the following sections, the additional reduction steps applied to the data presented here, the final calibration errors and the unresolved problems are described.

3.1.1. Additional reduction steps

In the AOT 01 mode, the grating scanner moves within one reset interval while the detectors are integrating. Hence, during a single integration, radiation of different wavelengths is observed and thus signal from line and continuum emission is mixed. As a result the slope of the integration ramp shows a change. When the contrast between the continuum signal and line signal is large enough, this will give such a sharp slope change that it is flagged as a glitch (i.e. cosmic ray hit) in OLP versions earlier then OLP10. Hence, in combining the detector measurements by rebinning the data, the peak of the line is not properly reconstructed due to the missing high flux samples. Hence, the total flux of the atomic line will be underestimated. In the present analysis, automatic glitch detection and removal was only applied in wavelength regions where

no line emission is expected. Afterwards, the line regions are checked manually for glitches at the AAR level. Since strong glitches left in the data will influence the average flux of the detectors, this is done for each detector separately before flat-fielding the detectors.

The Si:Ga detectors of band 2 and the Ge:Be detectors of band 4 exhibit memory effects. The detector responsivity is not constant and their response to a sudden flux change is not "instantaneous" with respect to the time resolution of the SWS read-outs. Both effects depend on the present illumination, the detector operating parameters (bias, temperature) and the illumination history during the last hours. Generally, compact H II regions have strong increasing continuum in this wavelength region. As a result memory effects strongly affect the shape of the underlying continuum. Especially when comparing the "up" and "down" scans, large differences are seen due to the fact that the "flux history" as perceived by the detectors is different for the two directions. This detector memory effect has been studied extensively by Fouks and Schubert who have proposed a model for the behaviour of the Si:Ga detectors (Fouks & Schubert 1995). For the band 4 Ge:Be detectors no satisfactory model has been established to date. For the SWS band 2 detectors, a detector memory effect correction algorithm based on the Fouks & Schubert formalism has been implemented (see Kester 2001). This algorithm was applied for all band 2 data. For the resulting corrected data generally the "up" and "down" scans agree within a few percent.

The flux calibration files were updated while reducing the sample sources (corresponding to the final post-mission calibration, OLP10; Shipman & Lahuis 2000). In order to get the final line fluxes, we multiplied the spectra and the measured line fluxes by a factor corresponding to the ratio of the used to the new flux scale calibration factors.

Within filter elements or within the detector material – especially for the band 3 detectors – multiple reflections between the element front and back surfaces may occur. The resulting interference fringes appear as a high frequency modulation of the detector output signal. To some extent all detector bands suffer from fringes. Bands 1, 2 and 4 are only lightly affected, whereas the fringes are more pronounced in band 3. These fringes can be corrected for by fitting cosine functions to the data in wavenumber space and dividing the observed fluxes by those functions. This procedure was applied for bands 3C, 3D and 3E, where the fringes are resolved. Only for the high resolution data of K3-50A fringes are also resolved and hence removed in band 3A.

The final reduction steps are applied at the AAR level. Strong glitches left in the spectra are removed manually (see above). The signals of the 12 detectors of a given AOT band are then all flat-fielded to the average level. Subsequently, for each resolution bin, the median and the standard deviation are calculated. Each point of which the deviation from the mean is more than 2.5 times the standard deviation is removed when situated in line-free spectral regions. Remaining bad data points are manually removed. Finally, all detector data are rebinned to a wavelength grid with a spectral resolution of ∼450.

In case of sources with no or low flux, the reduction process is simplified. Since the deglitching method only influences the flux of strong lines, deglitching is applied to these sources. Furthermore, for each resolution bin, the median and the standard deviation are calculated. Each point that deviates from the mean by more than 2.5 times the standard deviation is removed when situated in *all* spectral regions.

3.1.2. Final calibration accuracies

The final absolute flux scale accuracies for the calibrated SWS spectra are given in Table 2. For each AOT band the 1σ accuracy is given including the SWS absolute flux calibration error and the uncertainties in the synthetic stellar models used in establishing the absolute flux scale.

The intrinsic wavelength scale accuracy for SWS was established early on in the ISO mission to be better than $\lambda/\Delta\lambda \geq 5000$ (Valentijn et al. 1996). For the resolution of ∼450 of the data presented here, this corresponds to ≤10% of a resolution element. However due to the limited accuracy of the satellite pointing and the offset of the given coordinates from the source peak position in some cases, the sources are not always centred in the SWS aperture. Since the observed wavelength directly depends on the angle of incidence of the radiation on the grating, an offset position translates into a slight wavelength shift. Thus, satellite pointing errors lead to an increase in the wavelength error resulting in an overall wavelength accuracy of about 1/3 to 1/6 of a spectral resolution element.

3.1.3. Unresolved problems

For SWS, a few problems still remain in the calibration. These problems and their consequences for the data presented here are discussed in the following paragraphs.

Pointing errors Since the SWS sensitivity (given by the beamprofiles), is not uniform across the instrument aperture (see Salama 2000), a spatial offset will generally result in a lower flux than what would have been observed at the centre of the aperture. Such an offset can be due to pointing effects of the satellite, to incorrect coordinates of the centre of the source or due to the extent of sources. E.g. for extended sources, different positions corresponds to different sensitivities. Each AOT band has its own beamprofile (see Salama 2000).

Spurious spectral features During the calibration process, the RSRF was fine-tuned to fit three narrow features in band 2C (9–9.3 μm, 10.1 μm and 11.0 μm) and one feature in band 3A (12.3 μm) which are believed to be instrumental since they were seen in all sources with the same strength and width. Although corrected, the shape of the

RSRF in these regions is still less reliable than in the rest of the AOT band.

Band 2A For most sources, the noise in band 2A dominates the spectra in this wavelength region (see Fig. 8). The noise level in band 2A is considerably higher than for other bands. In addition, compact H II regions have a low flux continuum in this wavelength range.

Band 3 Due to insufficient suppression of different grating orders, some of the radiation at wavelengths of approximately 13 μm is transmitted through the optical path corresponding to the long wavelength band 3D. As a result of this leakage, the slope of the continuum in band 3D is not certain longwards of 26 μm.

Band 3E has a very small extent in wavelength causing difficulties in its calibration. This results in a significantly higher flux scale error of 23% (see Table 2) as well as in a relatively poor quality spectral responsivity curve. Thus, the overall shape in the band 3E continuum is not very reliable.

These two problems can lead to the appearances of spurious features which are sometimes mistaken for dust emission features (e.g. the 22 μm feature, Chan & Onaka 2000).

Incomplete removal of fringes Although the procedure for removing fringes is generally very successful in the centre of AOT bands, in some cases at the edges of a band some residual fringing is left. However, this does not significantly affect the measured line intensities. Some fringes are left in the spectrum K3-50A.

Overlap 2C-3A As can be seen in the spectrum of IRAS 12073, IRAS 15502, IRAS 18434, K3-50A and DR21 in Fig. 8, band 2C and band 3A do not show similar flux in their overlap region (between 12 and 12.7 μm). Poor matches between different AOT bands can often be understood from a combination of dark current uncertainties and a steep RSRF in the overlap region. Dividing the data by the RSRF, when the dark current subtraction was not done properly, will induce incorrect shapes in regions where the RSRF shows features or where the RSRF has a steep slope (i.e. at the ends of the bands). For band 2C, deviation of the intrinsic flux can be due to improper correction for memory effects. This should be seen when comparing the up and down scan. The resulting effect on the line flux of [Ne II] is however less severe than the aperture effect and the calibration error.

Band 4 As explained in Sect. 3.1.1, band 4 detectors suffer strongly from memory effects and to date no proper correction method has been devised. As a result, the continuum between 29 and 45 μm is not well reconstructed. The "up" and "down" scans in this wavelength range can show differences by as much as 30%. Even the signal level around some of the strong lines in this band is affected in that they show tails due to memory effects. To make things worse, the Ge:Be detectors of band 4 are much more sensitive to cosmic particle hits than the other bands. The resulting glitches are almost impossible to correct due to their tails caused by memory effects. As a consequence of these problems together, the shape of band 4 is uncertain, e.g. DR21 presents an extreme example (see Fig. 8) and the fluxes of lines in this band have relatively high errors (see Table 5).

Apart from the difficulty in the shape of the underlying continuum due to the detector memory effects and their interplay with the cosmic particle hits, there appear to be some features within band 4 which could be related to calibration problems in the RSRF. For this wavelength range, no well understood calibration sources have been found to date. As a result, the RSRF is entirely derived from preflight ground based tests, which means this curve is valid only for extended sources uniformly filling the SWS beam. It is suspected that the sharp "kink" around 33 μm as well as the plateau around the 33.47 μm [S III] line are due to errors in the RSRF.

Once corrections for band 4 detector memory effects and/or a better responsivity curve become available the data will be re-analysed and better quality line fluxes can be published.

3.1.4. Remarks

A sinusoidal wave is present in the reduced spectrum of K3-50A in band 3A (see Fig. 8), as well as in the raw data. The origin of this wave is unclear to us.

The observation with TDT number 64600609 is plotted in the SWS region for W3 since the band overlaps are slightly better in this spectrum. For IRAS 22308, the SWS spectrum with TDT number 17701257 is shown, the LWS part has TDT number 17701258. Again, for the SWS part, this spectrum has a slightly higher quality. For LWS, we took the observation obtained immediately after the SWS observation plotted here. When comparing these two observations of the same source in the SWS wavelength regime, differences can be found since the orientation of the aperture is not the same and the source is extended. For the LWS regime, the aperture position and orientation is the same for both observations.

3.2. LWS reduction

The LWS observations are calibrated using the pipeline version 8.7. For a detailed description of the instrument and its reduction we refer to Swinyard et al. (1998) and the ISO Handbook volume IV: LWS – The Long Wavelength Spectrometer by Gry et al. (2000).

LWS data was calibrated following the standard reduction steps, which basically include: first-level deglitching, responsity drift and absolute response correction, dark

current substraction and finally, wavelength and flux calibration. These processes yield the Auto Analysis Result (AAR).

3.2.1. Additional reduction steps

The dark signal subtraction is a crucial step for very faint sources because a wrong subtraction can lead to negative photocurrent values and to large differences in the flux levels between the sub-spectra. Therefore, the faint sources were reprocessed with the LWS Interactive Analysis Software (LIA) in order to refine this process. LIA also allows us to redo the drift and absolute responsivity corrections, but these tools were not used as their improvement over the pipeline was found to be small.

The post-pipeline analysis of the AAR was performed with the ISO Spectroscopy Analysis Package (ISAP). First of all, the deglitching done in the pipeline removes a large part of the glitches, but some of them or their tails can remain in the data. Furthermore, some glitches may cause latency effects on the detector response which may cause part of a scan for one detector to be higher than the others for some period of time. ISAP permits the removal of these bad data. This step is followed by taking the average of all the 6 scans for every detector and the correction for fringes.

Fringes are caused by the interference of two beams (one beam arising from the normal reflection from the LWS field mirror and another from the support structure holding this mirror) which propagate along the instrument with a time delay between them. All detectors are in principle influenced, but the long wavelength detectors are most affected. Fringes occur in the spectra when the source is extended (i.e. $>20''$) and/or structured, or when a point-like source is mispointed or when a point-like source is observed against a strong background. The latter is common for sources that lie in the Galactic plane, such as H II regions. The fringes are then expected at the longer wavelengths where the intrinsic emission of the source decreases and becomes comparable to the Galactic background emission. These fringes affect the continuum as well as the [O I] and [C II] lines at 145 and 158 μm. They are corrected for in ISAP by dividing out a sinusoidal function with a wavelength dependent amplitude.

3.2.2. Final calibration accuracies

The intrinsic wavelength calibration accuracy achieved in the grating mode is better than 1/4 of a resolution element of the grating, i.e. 0.07 μm for the SW detectors and 0.15 μm for the LW detectors.

A 10% absolute flux uncertainty is a "reasonable" value for the majority of the LWS observations for all but the SW1 detector. The calibration of the SW1 detector is worse compared to the other detectors, yielding a higher absolute flux uncertainty. In case of very faint sources ($<$100 Jy at 100 μm), very bright sources ($>$50 000 Jy at 100 μm), extended sources with a complex morphology, sources not centred in the beam or sources observed against a strong background, the absolute flux uncertainty can be higher. An indicator for the latter is the scatter between adjacent detectors in the defringed and aperture corrected spectrum.

3.2.3. Unresolved problems

Differences between overlapping sub-spectra The continuum flux in the SW1 detector is on average $\sim$20% higher than the continuum flux in the adjacent detector, varying from about 50% for IRAS 05335 to a good agreement in the case of IRAS 18116. For the other detectors, the differences in flux in the overlapping regions are much lower, ranging from a few % up to 20% in a few cases.

Incomplete removal of fringes The routine in ISAP used to remove fringes worked successfully except in the case of some very strong sources (for instance IRAS 18434 and IRAS 19598) where a spurious broad feature centred at 127 μm with a *FWHM* of $\sim$2 μm is found in detector LW3. This broad feature causes an insufficient removal of fringes resulting in a poor determination of the continuum for the [O I] 145 μm line observed in this detector.

Spurious features Spurious features are found in most of the spectra at 112.0 μm (in detector LW2), at 141.8 μm and at 146.5 μm (the latter two in detector LW3). The former is identified as HD R(0); the emission at 146.5 μm almost blends with the [O I] emission line at 145 μm. These are probably absorption features of Uranus which appear as emission lines in the output product. In addition, there is a spurious broad feature centred at 127 μm, as discussed above.

Memory effects Memory effects, which appear as slope differences between both scan directions, are due to the different response of the detectors depending on whether the signal increases or decreases with time. SW1 is always affected by this problem. The other detectors are only troubled in the case of strong and intermediate sources. Detector SW2 is specially affected in strong sources, influencing the [O III] line at 51.8 μm. For intermediate sources, memory effects are mainly present, although in a much lower degree, in detectors LW2, LW3 and LW4. To date, no correction tool is available. Hence, both scan directions are reduced separately in order to quantify this effect.

Non-linear detector behaviour For very strong sources (of the order of 10 000 Jy), the long wavelength detectors (specially LW3) can have a non-linear response and saturate. As a result, the shape of the sub-spectra sags in the middle. Only detector LW3 in the strongest sources (e.g. IRAS 02219, IRAS 18434 and IRAS 19598) seems to be affected by this problem. A test on IRAS 19598 was made

by reprocessing the data with 1/4 second ramps. However, the overal shape of the LW3 detector, dominated by the spurious broad feature mentioned earlier, did not improve.

3.3. Extended source calibration

The SWS calibration (except the flux calibration of band 4) and LWS calibration are entirely based on point sources. To correct for source structure within the instrument beam at any given wavelength, the beam profile has to be convolved with the source brightness distribution. This correction can only be applied when the source structure is known *at all wavelengths in the spectrum, both for the continuum emitting regions and for the line emitting regions*. Such a detailed knowledge of the source structure is not available for any of the H II regions discussed in this paper.

In addition, for the LWS detectors, a substantial fraction of the flux from an on-axis point source is diffracted out of the aperture. Because the calibration is applied to point sources observed on axis, these losses are automatically corrected for. However, these diffraction losses do not occur in the case of extended sources and so the flux of these sources is overestimated.

The spectra have therefore been derived assuming that the sources are point-like for both SWS and LWS and on axis for LWS. The jumps occuring at the SWS band edges and/or at the junction of the SWS and the LWS spectra and/or at the overlap of two LWS detectors can be caused by this effect. The line fluxes listed in Tables 5–8, also assume that the sources are point-like and on axis. For extended sources, conversion factors (depending on the wavelength) should be applied to convert the fluxes from Jy to MJy/sr. The conversion factors for an *infinitely extended and homogeneously distributed* source at the key wavelength of each AOT band and LWS detector are given in Salama (2000) and can be applied, if desired, for both the spectra and the presented fluxes. These extended source correction factors are illustrative so caution should be taken when applying them.

4. Line fluxes

4.1. Gaussian fits

The fluxes of the lines in the SWS and LWS spectra are measured by fitting a Gaussian with the interactive line-fitting routine in ISAP. For the lines in the LWS spectrum, the *FWHM* of the Gaussian fits was kept fixed with a value equal to the spectral resolution element of the data (0.283 μm for lines in detectors SW1-5, and 0.584 μm for detectors LW1-5). The *FWHM* in the fit of the SWS lines was kept as a free parameter as it changes with wavelength. The line fluxes were measured in the independently reduced "up" and "down" scans and in the combined spectrum. The latter measurement gives an estimate of the statistical error of the line flux through the error in the fit. The difference in the line fluxes measured in the "up" and "down" scans, on the other hand, provides an estimate of the systematic error coming from memory effects and the uncertainty in the choice of the local continuum. The error listed in Tables 5–8 is the square root of the quadratic sum of these two errors (the calibration uncertainties are *not* included in these listed errors).

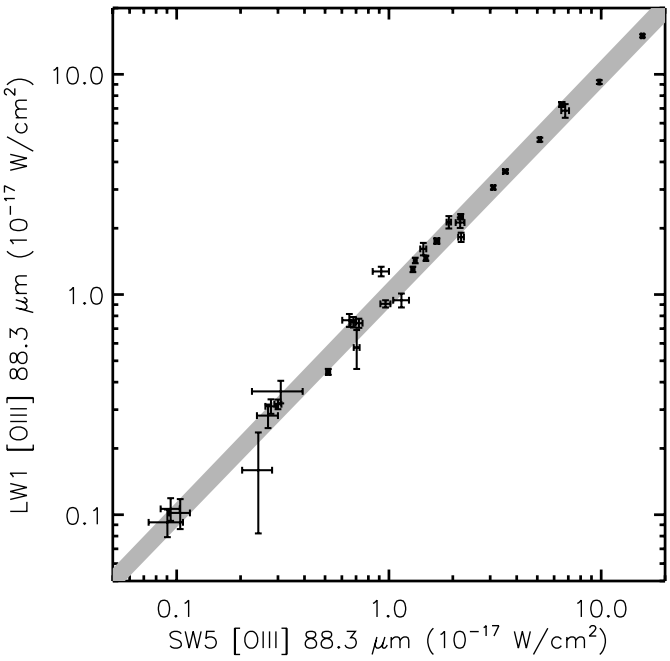

Fig. 1. Comparison of the [O III] 88.3 μm fine-structure line present in both the SW5 and the LW1 detector. The error bars correspond to the maximum of the fit error and the up-down error (see text). The grey band corresponds to the 10% calibration uncertainty expected for both detectors.

A line is defined as being detected if it is present in both the up and the down scan, its peak intensity is two or more times higher than the rms noise of the local continuum and when the line has a *FWHM* of the spectral resolution element. For any line which does not fulfil all these criteria, an upper limit for the flux is derived. The upper limits are defined as the flux of a feature with a peak flux three times the continuum rms noise and a width equal to the instrumental resolution element.

A few lines occur in the overlap region of two SWS AOT bands. Usually, one of each pair of lines is incompletely covered or fall outside the "official" wavelength range of the AOT band, where the sensitivity of the detector has dropped dramatically. Hence, the line in the other band is used. The lines in these overlap regions listed in Tables 5 and 7 are : Brβ in AOT band 1B, H I (10–5) and H I (9–5) in 1D, H I (8–5) in 1E, H I (14–6) and Brα in 1E and [Ar II] 7 μm in 2C.

For the LWS observations, some of the fine-structure lines were measured simultaneously by two adjacent detectors, e.g. the [O III] 88 μm line by the SW5 and LW1 detectors, and the [O I] 145 μm line by LW3 and LW4. For the sample of H II regions, the fluxes for the [O III] 88 μm line agree very well as shown in Fig. 1. Judging from Fig. 1,

the 10% calibration uncertainty associated with these detectors is a conservative estimate. The value quoted in Table 6 is the weighted mean flux of both lines. This has not been applied to the [O I] 145 μm line, for which only the line flux measured in detector LW4 is listed, as the line in detector LW3 is heavily affected by fringes and its local continuum is very difficult to determine.

4.2. Error budget

In order to calculate the final error on the line fluxes, a description of the errors that are involved, is given. First, by fitting the observed line with a Gaussian, a statistical error of the line flux is obtained through the error in the fit. Second, an additional error is obtained by the difference in the line fluxes measured in both the – independently reduced – up and down scans. Third, all SWS AOT bands and LWS detectors have an absolute flux uncertainty. This absolute flux uncertainty is discussed in Sect. 3.1.2 for SWS and in Sect. 3.2.2 for LWS. Fourth, all steps in the reduction process involve additional errors. Recently, a full error propagation is done for each detector flux for the applied SWS reduction process (implemented in the test version of IA by fall 2000). Since, this was not included in the pipeline at the time the reduction was done, this error estimate is not available. The total error on the line flux is generally dominated by the absolute flux uncertainty.

Errors on line ratios

For two lines in the same AOT band (for SWS) or in the same detector (for LWS), the uncertainty in the absolute flux will cancel out when taking a ratio of them. Hence, in this case, the final error on the line flux, used to calculate the error on the considered line ratio, will be the square root of the quadratic sum of the statistical error coming from the Gaussian fit and the error derived from the difference between the up and down scan measurements (i.e. the error listed in the Tables 5–8).

When the considered lines of a line ratio are observed in different SWS AOT bands or LWS detectors, the total error on each individual line flux must include the absolute flux uncertainty of the SWS AOT band or LWS detector in which the line is observed. In this case, the error, ϵ, on each individual line is based on the following formalism :

$$\epsilon = \sqrt{\epsilon^2_{\rm Gauss} + \epsilon^2_{\rm mem} + \epsilon^2_{\rm absflux}}$$

where $\epsilon_{\rm Gauss}$ is the statistical error coming from the Gaussian fit, $\epsilon_{\rm mem}$ is the error coming from the difference between the up and down scan measurements and $\epsilon_{\rm absflux}$ is the absolute flux uncertainty of the AOT band/detector that observed the considered line. In most cases, the error is dominated by the absolute flux uncertainty.

4.3. Influence of source morphology and size on the observed line fluxes

The extend and structure of some sources (see Sect. 6.2) influence the observed line fluxes in two ways. First, the aperture size changes with wavelength (see Sects. 2.2 and 2.3). Second, the morphology, the size of the source, the offset from the source peak position and the pointing error of the satellite are important for the observed flux due to the instrumental beam profiles (see Sects. 3.1.3, 3.2.3 and 3.3). Several sources, flagged in Tables 5 and 7, show offsets between the SWS pointing and the radio source peak position of more than 10″. Other sources (e.g. IRAS 17279) show complex structure. Hence, care should be taken in the interpretation and analysis of the data.

5. Comparison with other instruments

5.1. Comparison with KAO

For a number of H II regions in the present sample, fine-structure lines were measured with the KAO (see Table 3 for references). For the [O III] 51.8 and 88.3 μm and the [N III] 57.3 μm, the LWS line fluxes are systematically higher compared to the KAO fluxes (see Fig. 2). However, their ratio is smaller than the aperture ratio suggesting that the sources are more extended than the KAO beam but smaller than the LWS beam at these wavelengths. Analogous, for the [S III] 18.7 and 33.5 μm and [Ne III] 36.0 μm, the fluxes obtained by the KAO are higher compared to SWS suggesting that the sources are more extended than the SWS beam at those wavelengths (see Fig. 3).

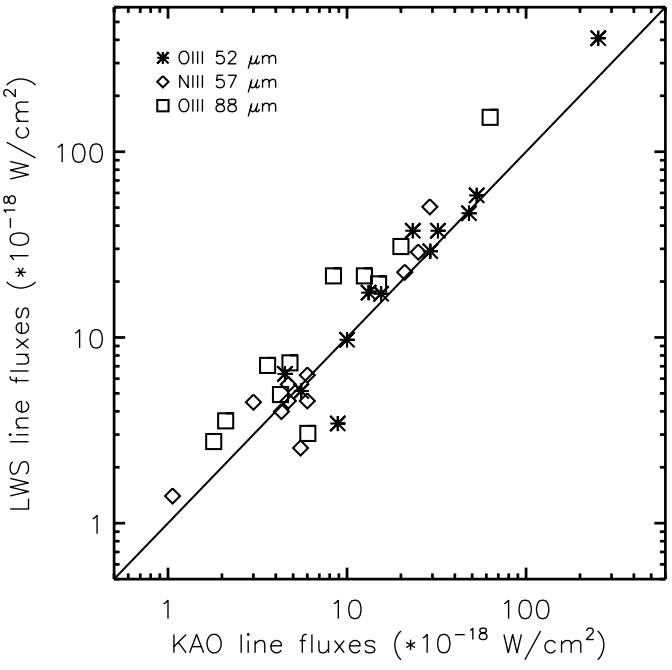

Fig. 2. Comparison of the LWS and KAO line fluxes for [O III] 51.8 μm, [N III] 57.3 μm and [O III] 88.3 μm fine-structure line. Beam size differences are *not* taken into account.

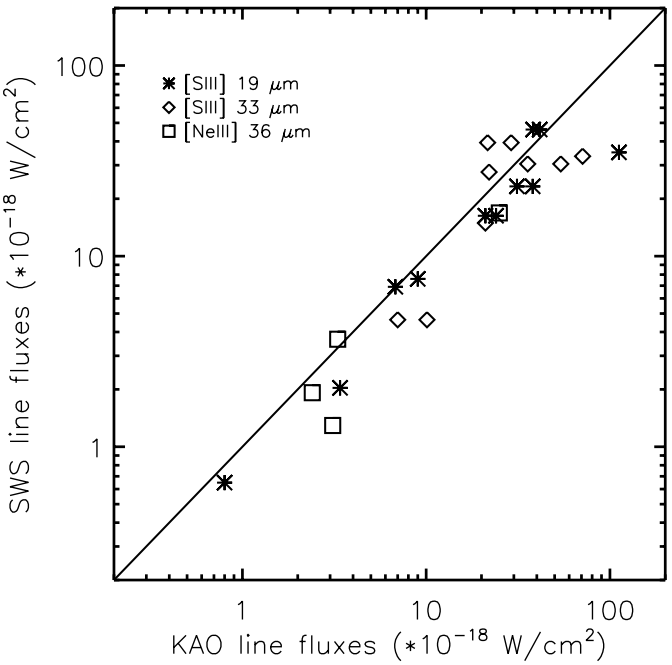

Fig. 3. Comparison of the SWS and KAO line fluxes for [S III] 18.7 μm, [S III] 33.5 μm and [Ne III] 36.0 μm fine-structure line. Beam size differences are *not* taken into account.

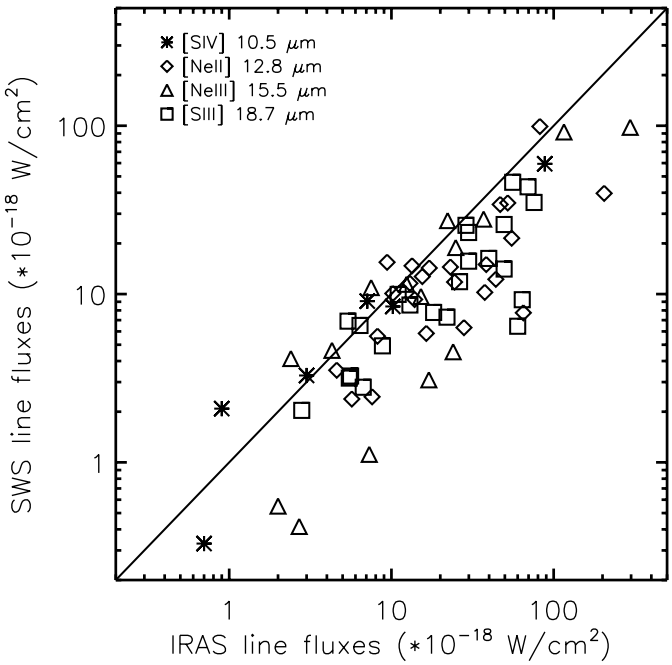

Fig. 4. Comparison of the SWS and IRAS line fluxes for [S IV] 10.5 μm, [Ne II] 12.8 μm, [Ne III] 15.5 μm and [S III] 18.7 μm fine-structure lines. The IRAS fluxes are taken from Simpson & Rubin (1990). Beam size differences are *not* taken into account.

Table 3. KAO observations.

Source	References
IRAS 01045	Rudolph et al. (1997)
IRAS 12073	Simpson et al. (1995)
IRAS 17455	Megeath et al. (1990); Simpson et al. (1995)
IRAS 17591	Afflerbach et al. (1997)
IRAS 18032	Afflerbach et al. (1997)
IRAS 18317	Simpson et al. (1995)
IRAS 18434	Herter et al. (1981); Megeath et al. (1990); Simpson et al. (1995)
IRAS 18479	Afflerbach et al. (1997)
IRAS 19110	Herter et al. (1981)
IRAS 19598	Megeath et al. (1990); Colgan et al. (1991)
IRAS 21270	Rudolph et al. (1997)
IRAS 21306	Rudolph et al. (1997)
IRAS 23030	Herter et al. (1982); Simpson et al. (1995)

5.2. Comparison with IRAS

Analogously, the [S IV] 10.5 μm, [Ne II] 12.8 μm, [Ne III] 15.5 μm and [S III] 18.7 μm fine-structure lines are compared with IRAS observations (see Fig. 4). The observed IRAS fluxes are systematically higher compared to the ISO fluxes due to its larger aperture. However, their ratio is smaller than the aperture ratio suggesting that the sources are more extended than the SWS beam but smaller than the IRAS beam at these wavelengths.

In addition, we compared the flux seen by ISO in the four IRAS bands at 12, 25, 60 and 100 μm with the corresponding IRAS PSC fluxes. The combined ISO SWS-LWS spectra are therefore used as they are observed. Hence, no correction is applied to the spectra. Figure 5 shows

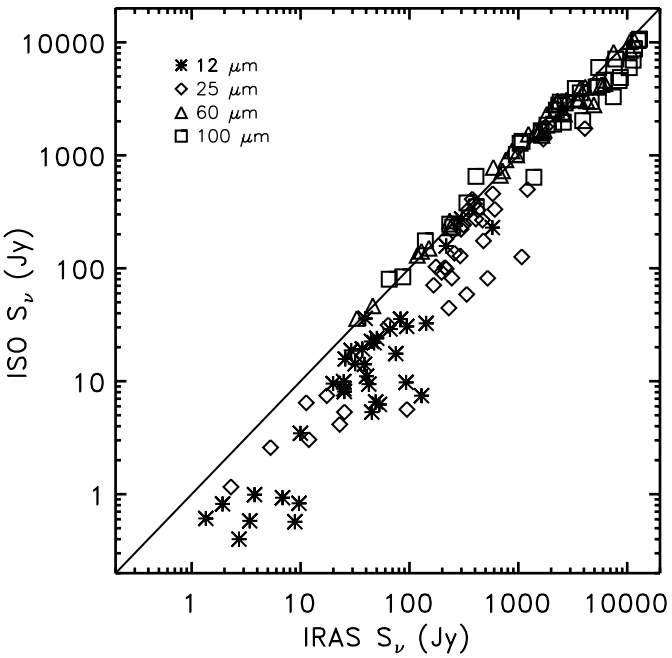

Fig. 5. Comparison of the IRAS PSC fluxes and the flux seen by ISO within the IRAS filters centred at 12, 25, 60 and 100 μm. Beam size differences are *not* taken into account.

clearly that the 60 and 100 μm filters give similar results for the IRAS PSC and ISO. For the 12 and 25 μm band filters, large differences are noted implying that the corresponding emission regions are larger then the ISO-SWS aperture.

6. Properties of the H II regions

6.1. Kinematic distances

Kinematic distances to the program H II regions were derived from velocities taken from the literature as detailed in Table 4. A flat Galactic rotation curve and the IAU standard galactic constants ($R_\odot$ = 8.5 kpc and $\theta_\odot$ = 220 km s^{-1}) were adopted. The kinematic distance to an H II region is best determined using velocities of radio hydrogen recombination lines. Where such data are available, they have been used. Where no recombination line data were available, the velocity information derived from molecular studies was used. In case of different molecular observations and/or various velocity components observed for one molecular species, we selected the velocity from a high density tracer with the following order of preference: CS, NH_3, H_2CO and CO.

Table 4 gives the selected tracer (Col. 1), its velocity (Col. 2), the derived galactic distance (Col. 3), the distance from the Sun, including the near and far distance for the sources in the inner solar circle, the latter one in brackets (Col. 5) and the list of references for the observed velocity (Col. 6). For sources within the solar circle there is always an ambiguity in determining the distance to the Sun due to the fact that there is a "near" and a "far" intersection of the line of sight with the orbit of the source around the Galactic Centre giving the same radial velocity.

For IRAS 12331, IRAS 18502 and IRAS 19207, the Galactic rotation model is not giving the measured $V_{\rm lsr}$, indicating that these H II regions deviate from the model. Here, the most probable estimate of the solar distances is given, i.e. the distance of the tangent point providing the closest $V_{\rm lsr}$ to the observed one. The radio recombination line obtained towards IRAS 17591 has a very complex profile and the derived distance is very sensitive to the exact velocity. Hence, we have followed Bronfman et al. (1996) and assigned a distance of 5.5 kpc derived from CS observations.

Figure 6 shows the location of the H II regions from Table 1 projected into the Galactic plane and Fig. 7 shows their distribution as a function of galactocentric distance ($R_{\rm gal}$), using the adopted distances from Table 4. The nebulae are distributed in the Galactic plane from the centre out to 22 kpc. Whereas the Galactic disk is well sampled between 3 and 12 kpc, fewer sources were observed in the inner regions and in the outer Galaxy.

6.2. Morphology

Despite the selection criterion that program sources should be point-like, many sources were found to be extended during follow-up studies. In part, this is due to the fact that the selection was often only based on IRAS data which has a limited spatial resolution. Recent radio observations show that the morphology of the selected H II regions is more complex than originally suspected and that some of the sources show structure at the size scale of the SWS apertures. The fact that some of the nebulae are extended and structured makes the interpretation of the ISO spectral data less straightforward than in the case of a point-like source. The main reason is that in the combined SWS-LWS spectrum the aperture size changes over the entire wavelength range from $14'' \times 20''$ for SWS band 1A to $\sim 86''$ diameter for LWS detector SW3. As a result

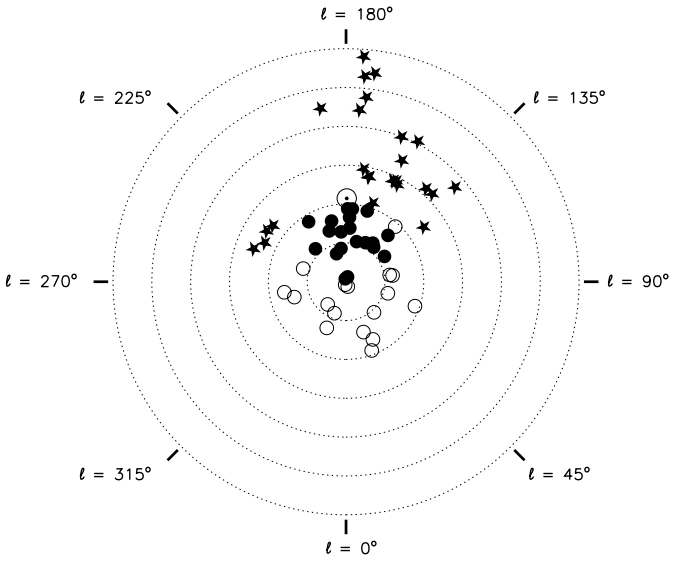

Fig. 6. Distribution over the Galactic plane of the H II regions listed in Table 1 (using the kinematic distances from Table 5). Distances to the Galactic Centre are indicated by concentric circles from 4 to 24 kpc by steps of 4 kpc. The position of the Sun (at 8.5 kpc) is shown by the ⊙ symbol. ⋆: sources beyond the solar circle; •: sources in the solar circle using the near distance; ○: sources in the solar circle using the far distance.

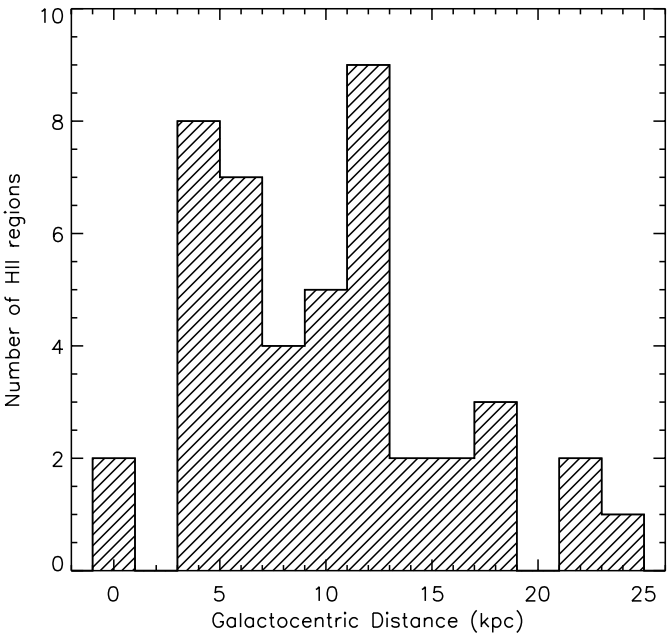

Fig. 7. Distribution of the H II regions as a function of galactocentric radius ($R_{\rm gal}$).

Table 4. Properties of the H II regions.

Source	Tracer	Distances $V_{\rm LSR}$ (km s^{-1})	$D_{\rm gal}$ (kpc)	$D_\odot$ (kpc)	Ref.	Morphology morpho-logy	Size[a]	Off[b]	Ref.	Luminosity $L/L_\odot$[c] (10^4)	
IR 01045	H42α	−69.3	13.8	7.0	1	spherical	3	3	1, 12, 21	4.11	
IR 01420	CO	−81.9†	16.3	9.5	2, 3	spherical	21	2	21	2.86	
IR 02219	H66α	−36.5	11.0	3.3	1	shell	35	0	1, 22, 23	52.9 $\natural$	
IR 02383	CO	−71.5†	15.8	8.6	2, 3	cometary	28	15	21	2.67	
IR 02575	CS	−38.0	11.5	3.6	4	complex$^\flat$	<7	0	24	2.96	
IR 04025	CO	−60.2†	18.5	10.7	2, 3	-	-	-	-	1.27	
IR 05167	CO	−26.3	21.7	13.3	3	-	-	-	-	1.65	
IR 05221	CS	−25.5	17.7	9.3	4	-	-	-	-	2.51	
IR 05302	CO°	−20.0	21.2	12.8	3	-	-	-	-	0.36	
	CO°	−10.3	12.3	3.8	3					0.03	
IR 05335	CO	−17.3†	23.2	13.3	3	-	-	-	-	1.24	
IR 06158	CO	+31.3†	18.0	9.7	2, 3, 5	complex	60	11	25	5.29	
IR 10589	H109(110)α	+22.0	9.5	8.0	6	cometary	7	5	26	29.4	
IR 11143	H109(110)α	+25.0	9.7	8.0	6	complex	48	9	26	14.2 $\natural$	
IR 12063	H109(110)α	+16.0	9.3	9.5	6	complex	9	2	26	45.0	
IR 12073	H109(110)α	+31.0	10.1	10.8	6	core-halo$^\flat$	7	6	26	400	
IR 12331	H109(110)α	−42.0	6.9	4.5	6	complex	50	15	26	8.45	
IR 15384	H109(110)α	−39.0	6.4	2.7 (11.5)	6	cometary	15	3	26	10.1	(183)
IR 15502	H109(110)α	−97.0	4.6	6.0 (8.4)	6	spherical$^\flat$	4	5	26	96.0	(188)
IR 16128	H109(110)α	−55.0	5.5	3.7 (11.4)	6	complex	12	17	26	22.8	(216)
IR 17160	H109(110)α	−69.0	3.0	5.7 (11.0)	6	complex	10	19	26, 27	35.6	(133)
IR 17221	H109(110)α	−21.0	5.2	3.4 (13.4)	6	complex	60	16	26	7.52	(117)
IR 17279	H109(110)α	−33.0	3.4	5.1 (11.8)	6	complex$^\flat$	8	6	26, 27	10.4	(55.9)
Sgr C	H70α	−65.5	0.3	8.2 (8.8)	7	complex	120	0	7	$\triangleleft$	
IR 17455	H70α	−19.6$^\diamond$	0.2	8.3 (8.7)	8	core-halo	14	0	27, 28, 29	49.2	(54.1)
IR 17591	CS	+15.4	5.5	3.0 (13.8)	4	complex$^\flat$	8	0	1, 27, 28	2.04	(43.1)
IR 18032	CS	+4.6†	7.6	1.0 (15.8)	4, 9	cometary$^\flat$	15	0	27, 29, 30	0.99	(249)
IR 18116	H92α	+51.9	4.3	4.5 (12.0)	10	cometary	20	0	27, 28	18.6	(132)
IR 18162	CO	+11.9†	6.6	1.9 (14.7)	11, 12, 13	core-halo$^\flat$	5	2	12	2.43 $\natural$	(146) $\natural$
IR 18317	H76α	+80.0	4.5	4.9 (10.6)	14	complex	13	10	27	14.7	(69.0)
IR 18434	H76α	+95.3	4.6	5.7 (9.0)	14	cometary$^\flat$	7	0	27, 30, 31	70.9	(177)
IR 18469	CS	+87.2†	4.8	5.3 (9.2)	4, 9	core-halo$^\flat$	13	0	27	11.1	(33.4)
IR 18479	H66α	+15.3*	7.5	1.2 (13.1)	1	complex$^\flat$	7	0	1, 27, 28	1.26	(150)
IR 18502	H76α	+100.0†	5.7	7.1	14	core-halo	6	0	27, 28	19.6	
IR 19207	H109α	+67.2	6.1	5.7	15	complex	140	0	32	38.4	
IR 19442	CS	+22.5†	7.6	2.5 (5.8)	4, 9, 16	spherical$^\flat$	1	0	33	5.30	(28.5)
IR 19598	H110α	−27.5	9.8	8.5	17	arc-like $^\flat$	4	0	1, 17, 34	201	
DR 21	H76α	−1.4	8.6	2.8	18	complex	20	0	18	$\triangleleft$	
IR 21190	H76α	−72.1	12.7	8.9	19	shell	4	0	35	21.4	
IR 21270	CO	−93.4†	14.8	11.3	3, 20	complex$^\flat$	120$^\flat$	25	21, 25	7.60	
IR 21306	CS	−71.1	12.6	8.3	4	complex$^\flat$	$^\flat$	18	36, 37	12.1	
IR 22308	CS	−52.1	11.3	5.5	4	cometary	90	0	25	6.99	
IR 23030	CS	−52.1	11.4	5.2	4	complex	40	8	37	10.5	
IR 23133	CS	−56.3	11.7	5.5	4	spherical	15	4	37, 38	18.5	

[a] Approximate source size in arcsec. [b] Approximate offset in arcsec between the source peak and the ISO pointing direction. [c] The luminosity corresponding with the far distance is given in brackets. ° 2 CO components found. No other molecular tracer available. * Complex source: velocity corresponds to the averaged value of the components (velocity differences of 2.5 km s^{-1}). † Averaged velocity from the different references $^\diamond$. Velocity forbidden in the sense of Galactic rotation. A distance of 0.2 kpc is assumed (Mehringer et al. 1998; Lis 1991). $^\flat$ See text. $\triangleleft$ No IRAS fluxes available. $\natural$ Upperlimits.

REFERENCES: (1) Afflerbach et al. (1996), (2) Brand & Wouterloot (1994), (3) Wouterloot & Brand (1989), (4) Bronfman et al. (1996), (5) Fich & Blitz (1984), (6) Caswell & Haynes (1987), (7) Liszt & Spiker (1995), (8) Liszt (1992), (9) Plume et al. (1992), (10) Garay et al. (1994), (11) de Vries et al. (1984), (12) McCutcheon et al. (1991), (13) Shepherd & Churchwell (1996), (14) Wood & Churchwell (1989), (15) Reifenstein et al. (1970), (16) Anglada et al. (1996), (17) Roelfsema et al. (1988), (18) Roelfsema et al. (1989), (19) Walmsley et al. (1981), (20) Blitz et al. (1982), (21) Rudolph et al. (1996), (22) Roelfsema & Goss (1991), (23) Tieftrunk et al. (1997), (24) Carpenter et al. (1990), (25) Fich (1993), (26) Martín-Hernández (2001), in prep., (27) Becker et al. (1994), (28) Garay et al. (1993), (29) Mehringer et al. (1998), (30) Cesaroni et al. (1994), (31) Fey et al. (1995), (32) Mehringer (1994), (33) Barsony (1989), (34) De Pree et al. (1994), (35) Isaacman (1984), (36) Ho et al. (1981), (37) Fich (1986), (38) Kurtz et al. (1999)

the region of the extended nebula seen by ISO will be a function of wavelength. In addition, the morphology, size of the sources, the offset from the source peak position and the pointing error of the satellite are important for the observed flux, as mentioned in Sects. 3.1.3 and 3.2.3. Table 4 gives an overview of these characteristics for each source in order to estimate whether these effects may be important. The source morphology and size derived from radio data are given in Cols. 7 and 8, respectively. The morphology classification is based on work by Wood & Churchwell (1989). Column 10 gives the approximate offset between the centre of the source and the ISO pointing direction. For those sources not mentioned in the table, no radio information is available in the literature.

Notes on individual sources

IRAS 02575: Kurtz et al. (1994) found 2 components: A (3.8″, core-halo) and B (1.1″, unresolved). The ISO observations are centred on source A. The ISO apertures contain both a compact H II region and a YSO. *IRAS 12073:* weaker components are found in both SWS and LWS beams (Martín-Hernández et al. 2001, in preparation). *IRAS 15502:* weak, unresolved companions are present in the beam (Martín-Hernández et al. 2001 in preparation). *IRAS 16128 & IRAS 17160:* the ISO pointing is at the edge of the source, excluding large regions in the smaller apertures (Martín-Hernández et al. 2001 in preparation). *IRAS 17279:* the ISO pointing is at the edge of the source, excluding large regions in the smaller apertures. Weak, unresolved companions are present in the beam (Martín-Hernández et al. 2001 in preparation). *IRAS 17591:* the ISO pointing is centred on component C (Garay et al. 1993; Afflerbach et al. 1996). *IRAS 18032:* ISO is centred on component B (Garay et al. 1993; Cesaroni et al. 1994). *IRAS 18162:* is a star forming region. Contains beside a compact H II region also a YSO. *IRAS 18434:* Fey et al. (1995) found extended emission (∼22″) at 1.3 cm. Observations at 21 cm by Kim & Koo (2001) found two strong components embedded in an extended emission (∼6′). *IRAS 18469:* Kurtz et al. (1994) found two unresolved components. Extended emission of ∼60″ is found by Kurtz et al. (1999). *IRAS 18479:* Kurtz et al. (1994) found 4 components. Extended emission (∼20″) is found by Kurtz et al. (1999). *IRAS 19442:* extended emission of ∼45″ is found (Barsony 1989; Kurtz et al. 1999). *IRAS 19598:* the object is not isolated. De Pree et al. (1994) found extended emission (∼17″). *IRAS 21270:* the ISO pointing is in between two sources. The given size correspond to the complete complex. The given offset is the offset of the ISO pointing from the closest component. *IRAS 21306:* the ISO pointing is in between two sources. The given offset is the offset of the ISO pointing from the closest component.

6.3. Luminosity

The FIR luminosities are determined by fitting a blackbody through the IRAS fluxes at 25, 60 and 100 μm taken from the Point Source Catalogue. The applied IRAS colour corrections are those for a source radiating like a blackbody. The derived luminosities are given in Table 4.

We choose to derive the luminosities in this way for the following reasons. First, one could consider integrating the full ISO SWS-LWS spectrum. However, due to the combination of the different aperture sizes within SWS/LWS resp. and between SWS and LWS on one hand and the extend of our sources on the other hand, different regions are looked at within different aperture sizes. Hence, only for point-like sources, the full ISO SWS-LWS spectrum reflects the SED of the source over the total wavelength range, i.e. from 2.3 to 196 μm. For extended sources, one can not compare straightforward the obtained spectra in different aperture sizes. When integrating the LWS spectrum only, the short wavelength contribution (<45 μm), which is a significant fraction of the total luminosity, is ignored. By fitting a (modified) blackbody to the LWS spectrum, the peak of the blackbody is not well defined causing large uncertainties in the derived luminosities. Finally, the IRAS flux at 12 μm is ignored since many features beside the dust continuum attribute to this filter.

Depending on which IRAS ratio (i.e. $f_\nu(25)/f_\nu(60)$, $f_\nu(25)/f_\nu(100)$ or $f_\nu(60)/f_\nu(100)$) is taken, a different temperature is derived for this blackbody and hence different colour corrections. This influences the derived luminosity by less than 4%. In general, the FIR spectra of H II regions are not perfect blackbodies but rather a combination of (modified) blackbodies at different temperatures. Derivation of the luminosity assuming that the source radiates like a single temperature modified blackbody gives a difference of less then 7% with those derived by assuming a blackbody. The error on the derived luminosities is dominated by the absolute flux calibration of IRAS, i.e. 30%.

The IRAS fluxes $f_\nu(60)$ for IRAS 21190 and $f_\nu(100)$ for IRAS 11143 and IRAS 18116 are upper limits. Hence, the derived luminosities for those sources are also upper limits.

7. The catalogue of combined SWS-LWS spectra

We present in Fig. 8, the combined SWS-LWS spectra from 2.5 to 196 μm of all the H II regions observed in the survey (see Table 1). In each panel of these figures, combined SWS–LWS spectra of three H II regions are presented. Each spectrum is labelled with the name of the source and the position of the atomic fine-structure lines, the hydrogen recombination lines and the dust bands are indicated at the bottom of each panel together with those wavelengths at which an aperture jump occurs. Note that in order to show the general shape of the dust emission bands and the continuum, the (strong) atomic lines have been cut off at the top in some of the spectra. As explained in Sect. 3, the spectra presented in Fig. 8 are not corrected for jumps occurring at the SWS band edges, at the limit between the SWS and the LWS or between the LWS detectors. The parts of the spectra corresponding to the poorly calibrated SWS Bands 3E and 4, the leak in

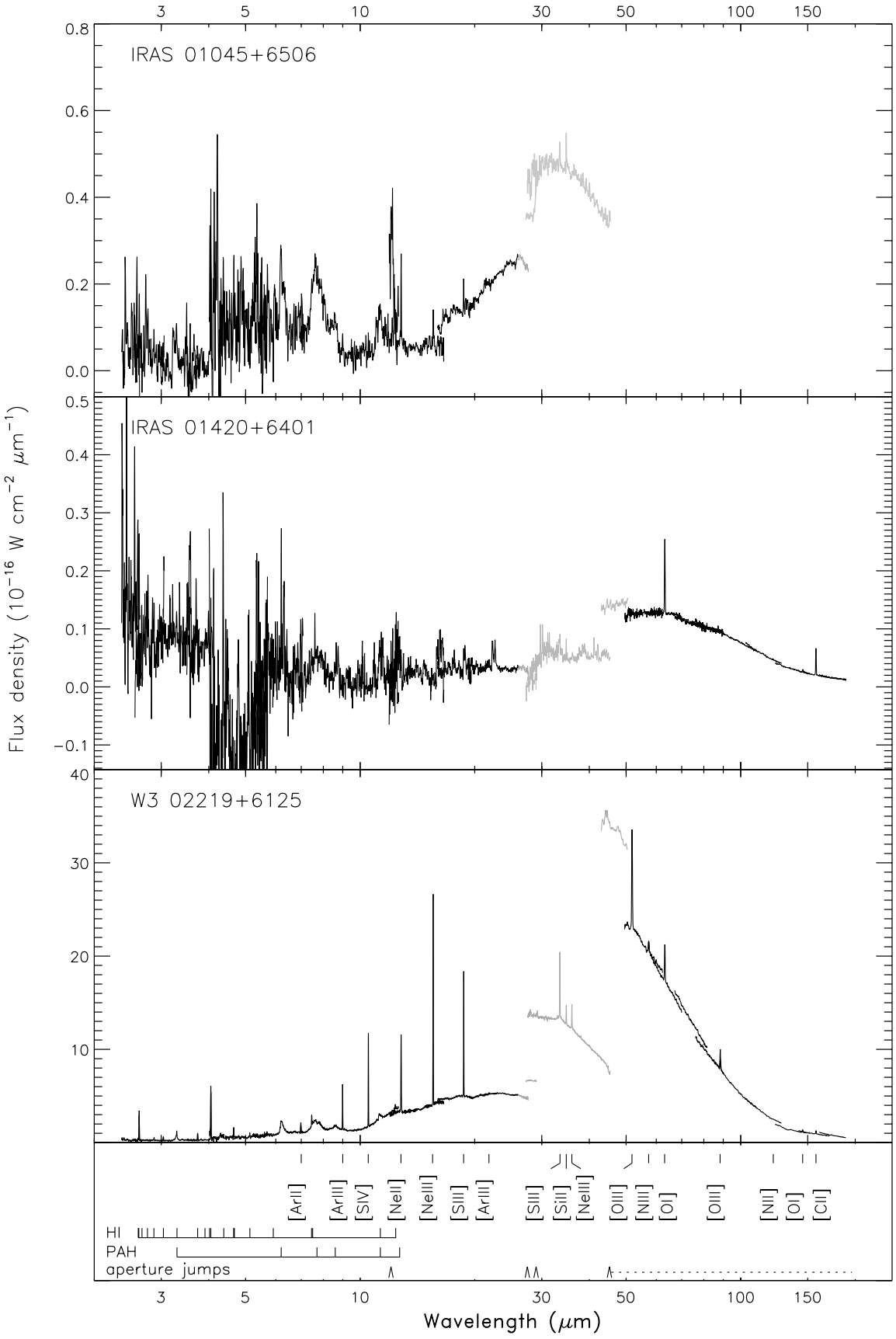

Fig. 8. The combined SWS-LWS spectra. The fine-structure lines, the hydrogen recombination lines and the main PAH features are identified. The wavelengths at which an aperture jump occurs within the SWS wavelength region and the wavelength between the two spectrometers SWS and LWS, are indicated by flags. The diameter of the LWS beam smoothly changes, ranging from 67″–85″, indicated by the dotted line.

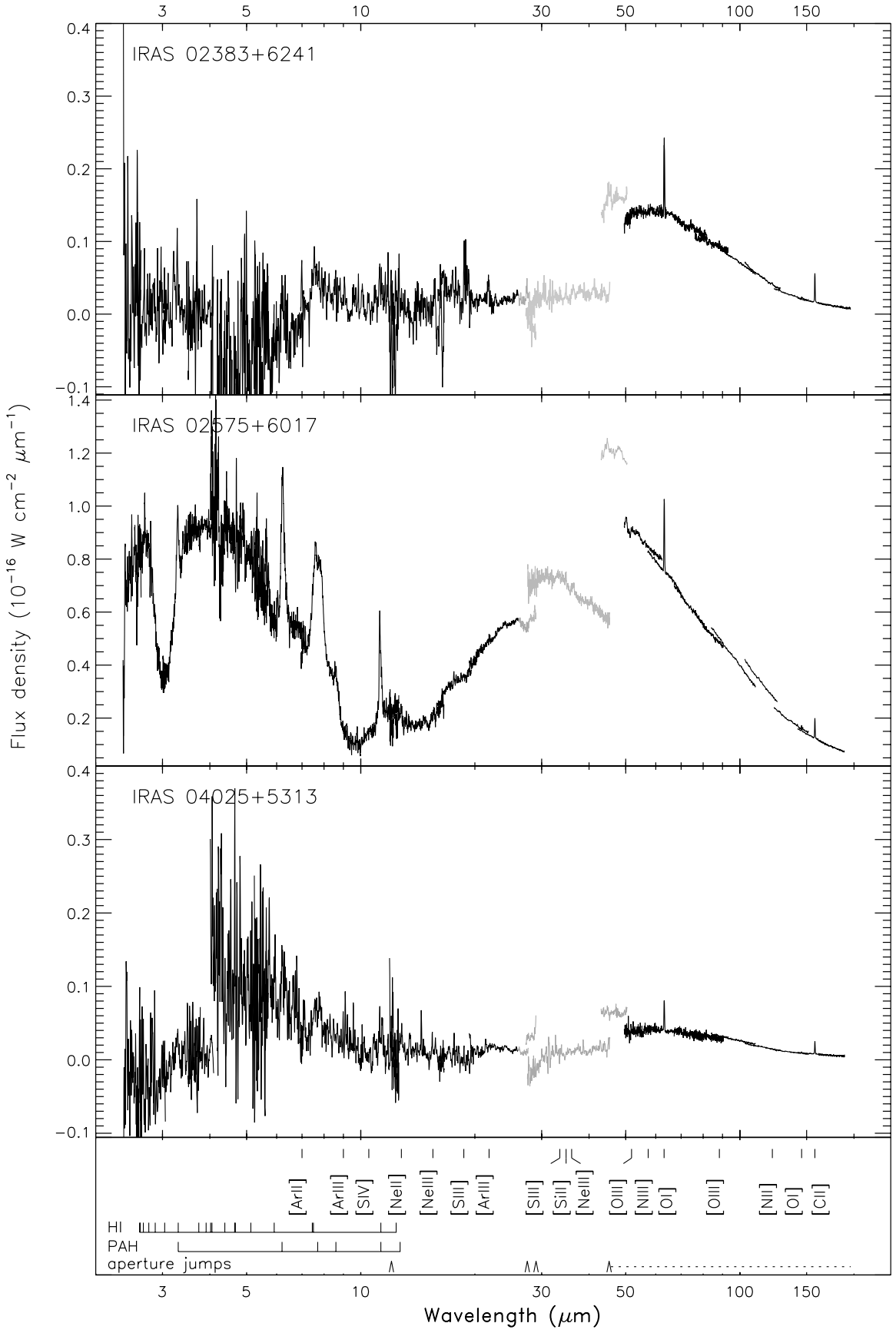

Fig. 8. continued.

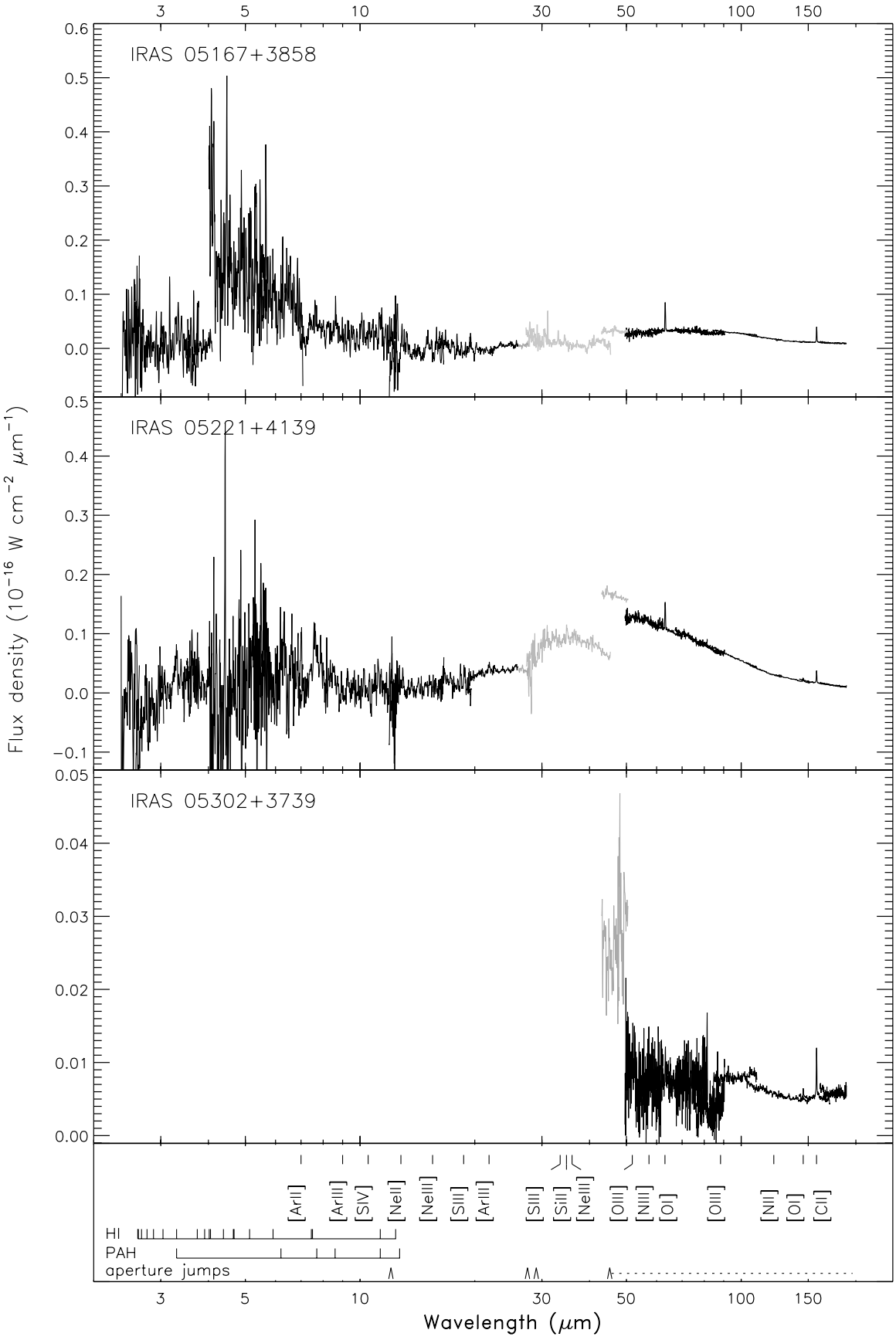

Fig. 8. continued.

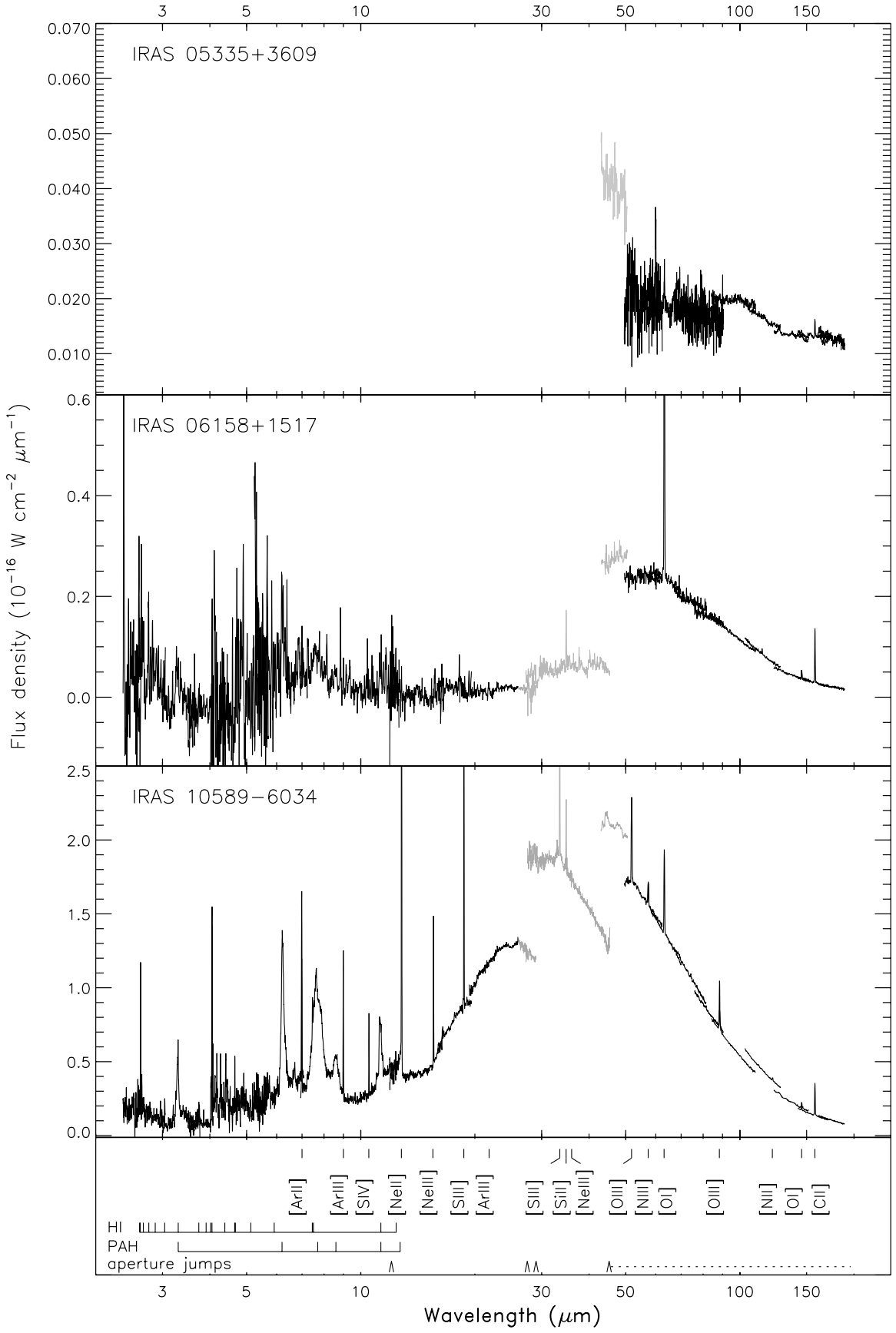

Fig. 8. continued.

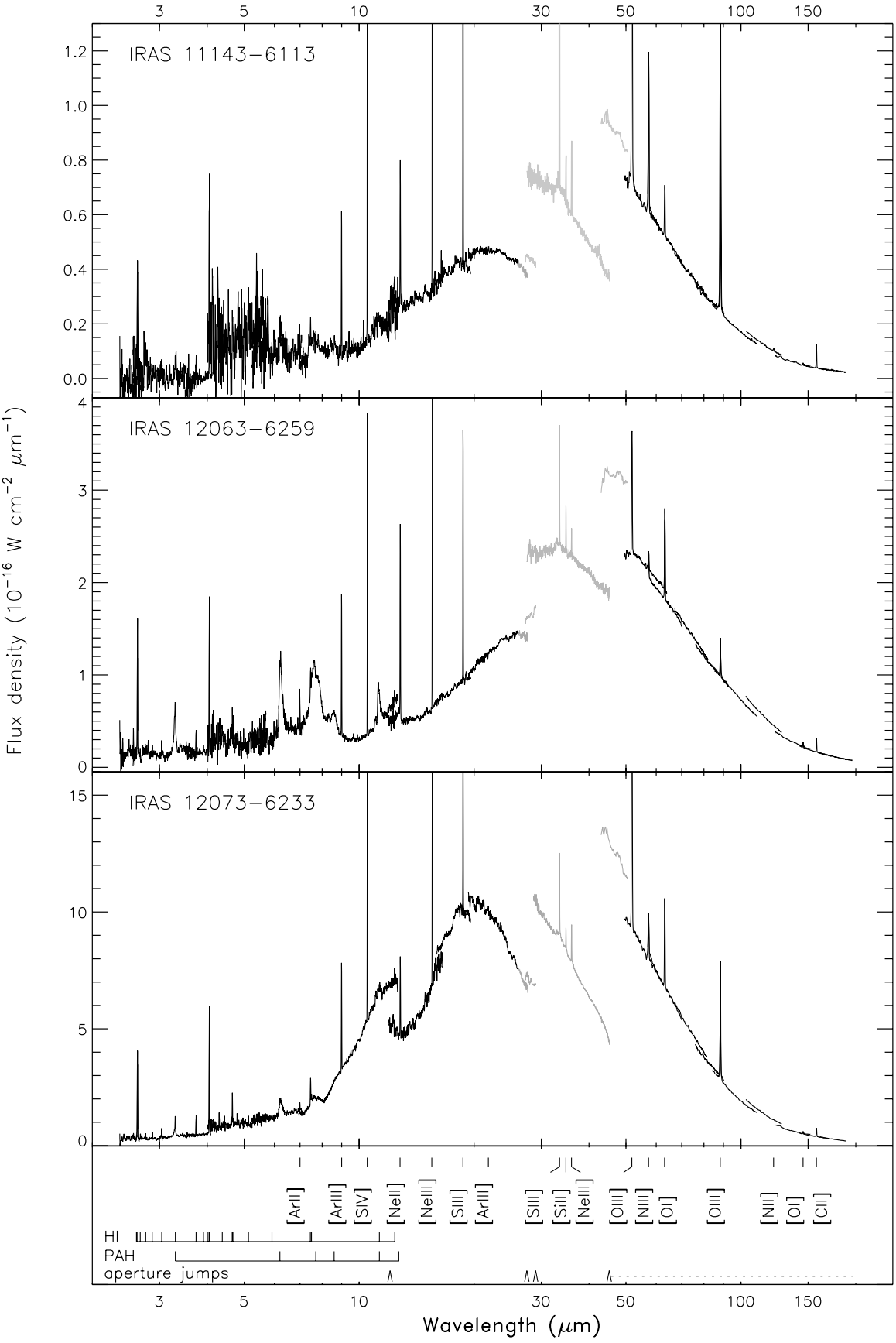

Fig. 8. continued.

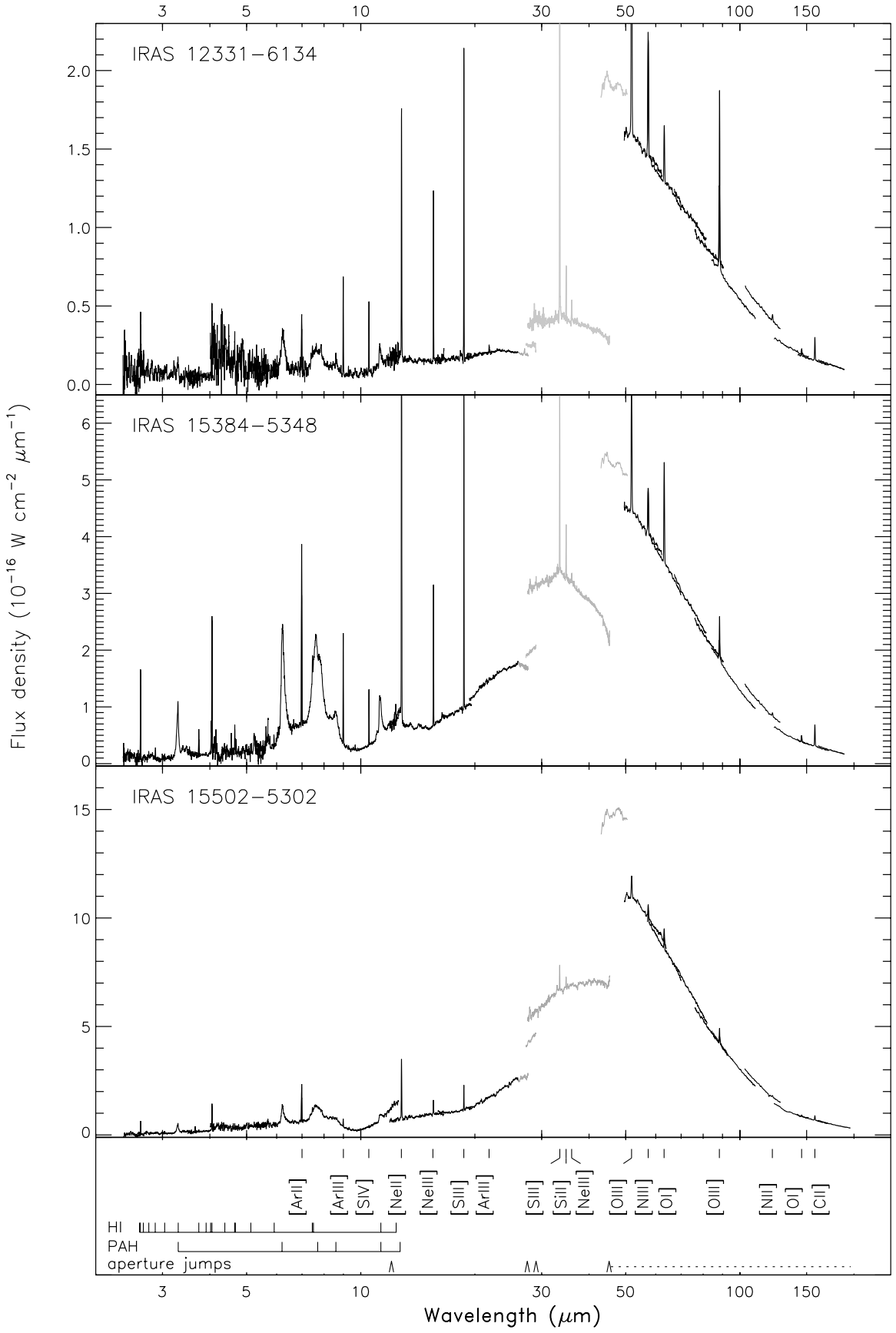

Fig. 8. continued.

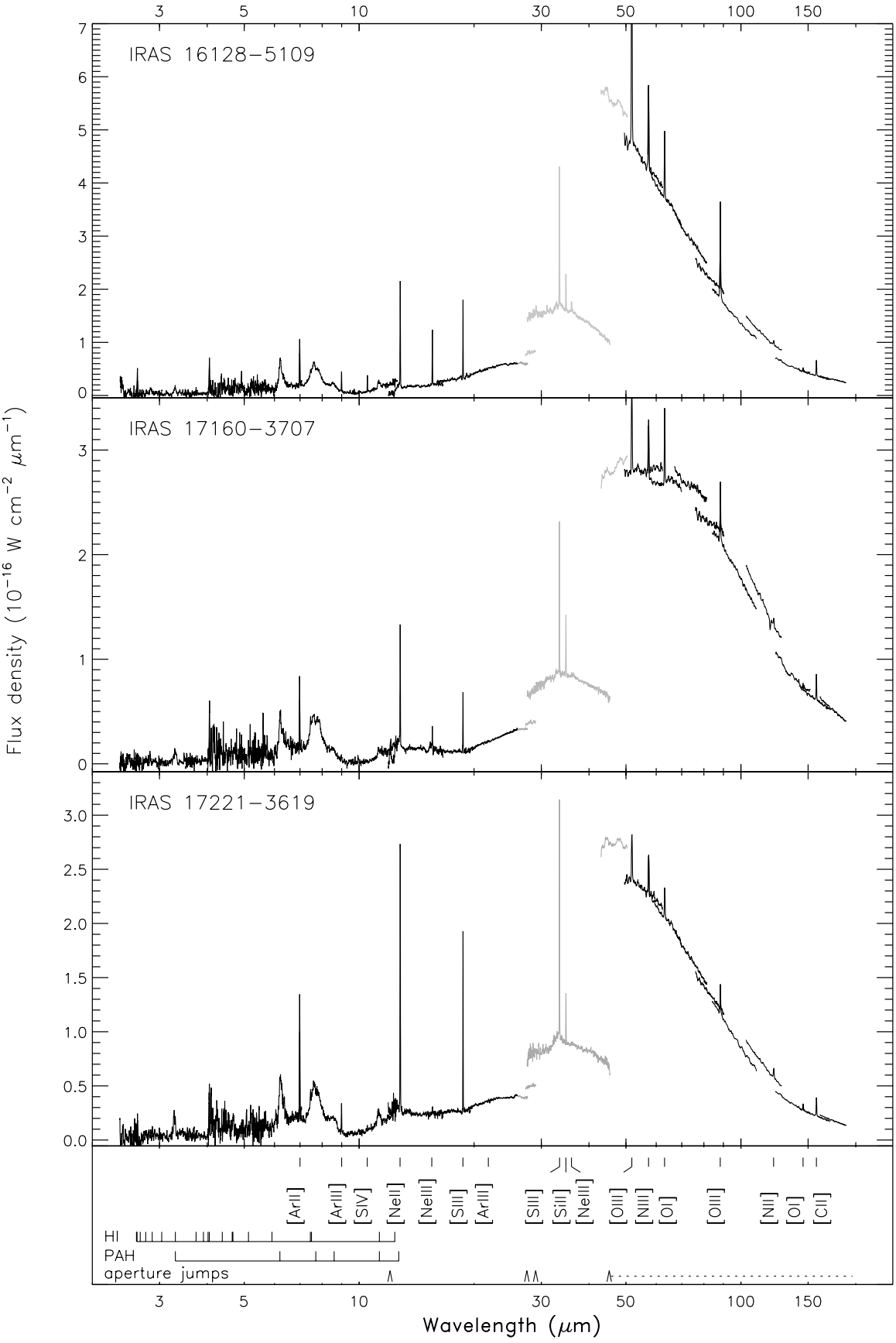

Fig. 8. continued.

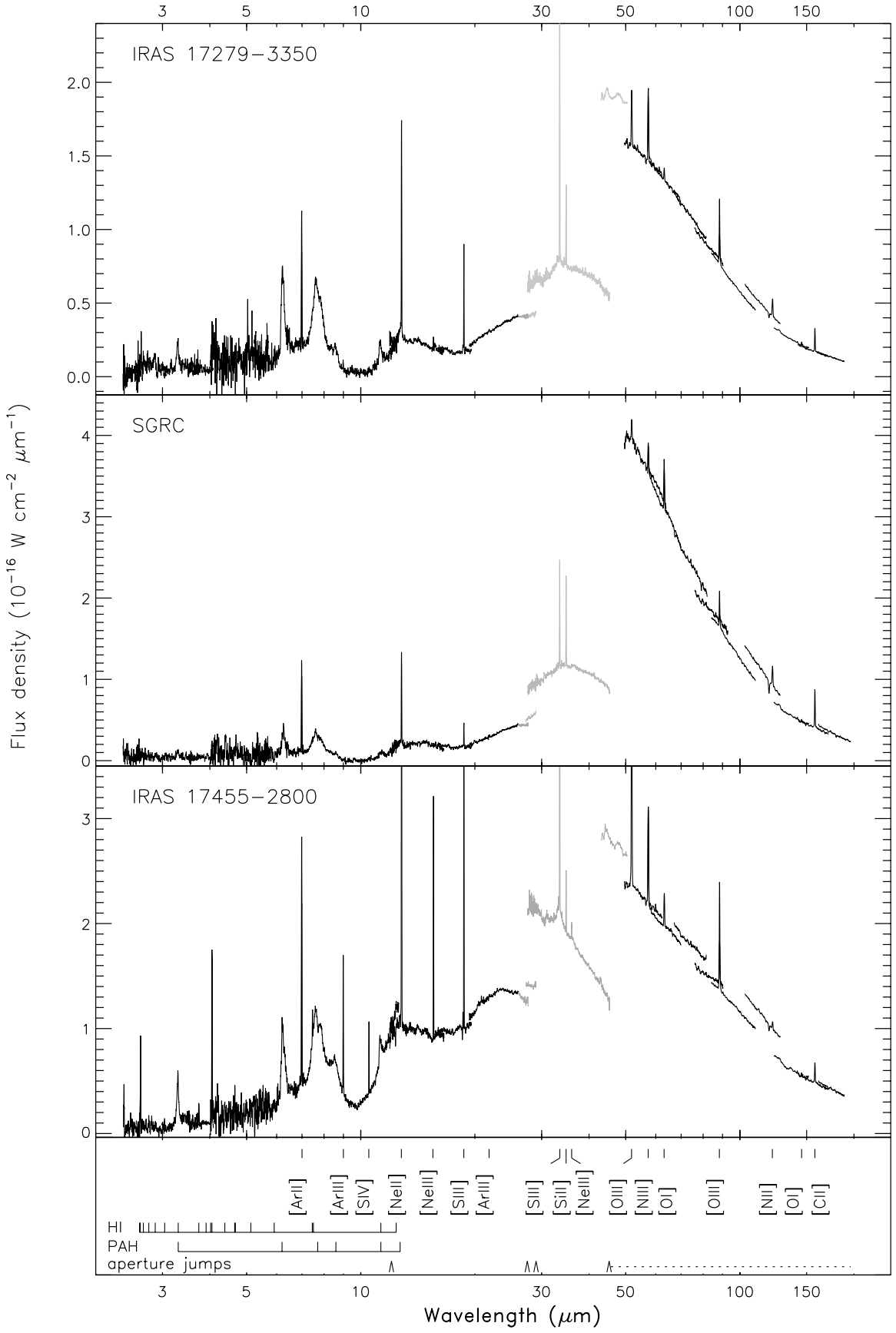

Fig. 8. continued.

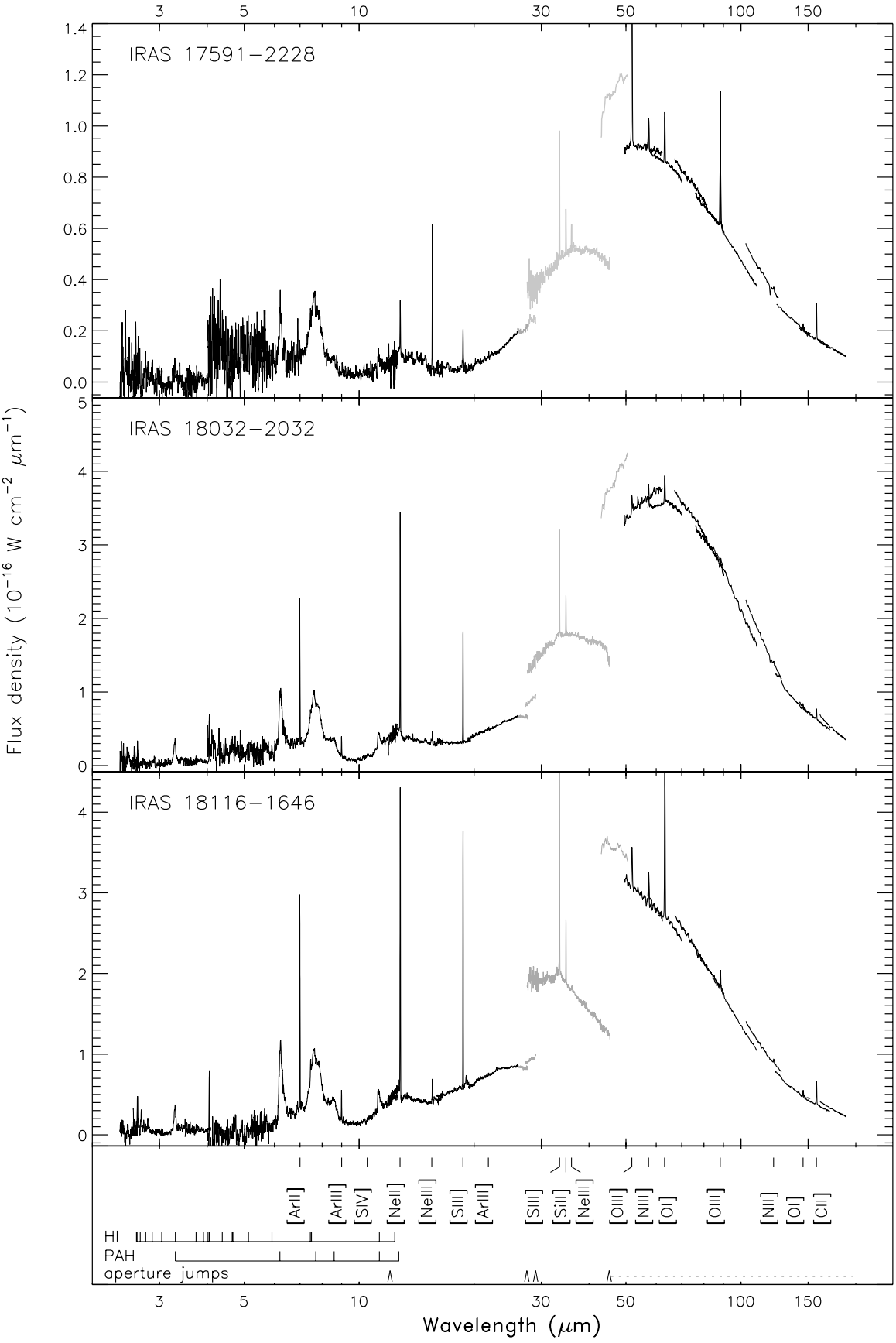

Fig. 8. continued.

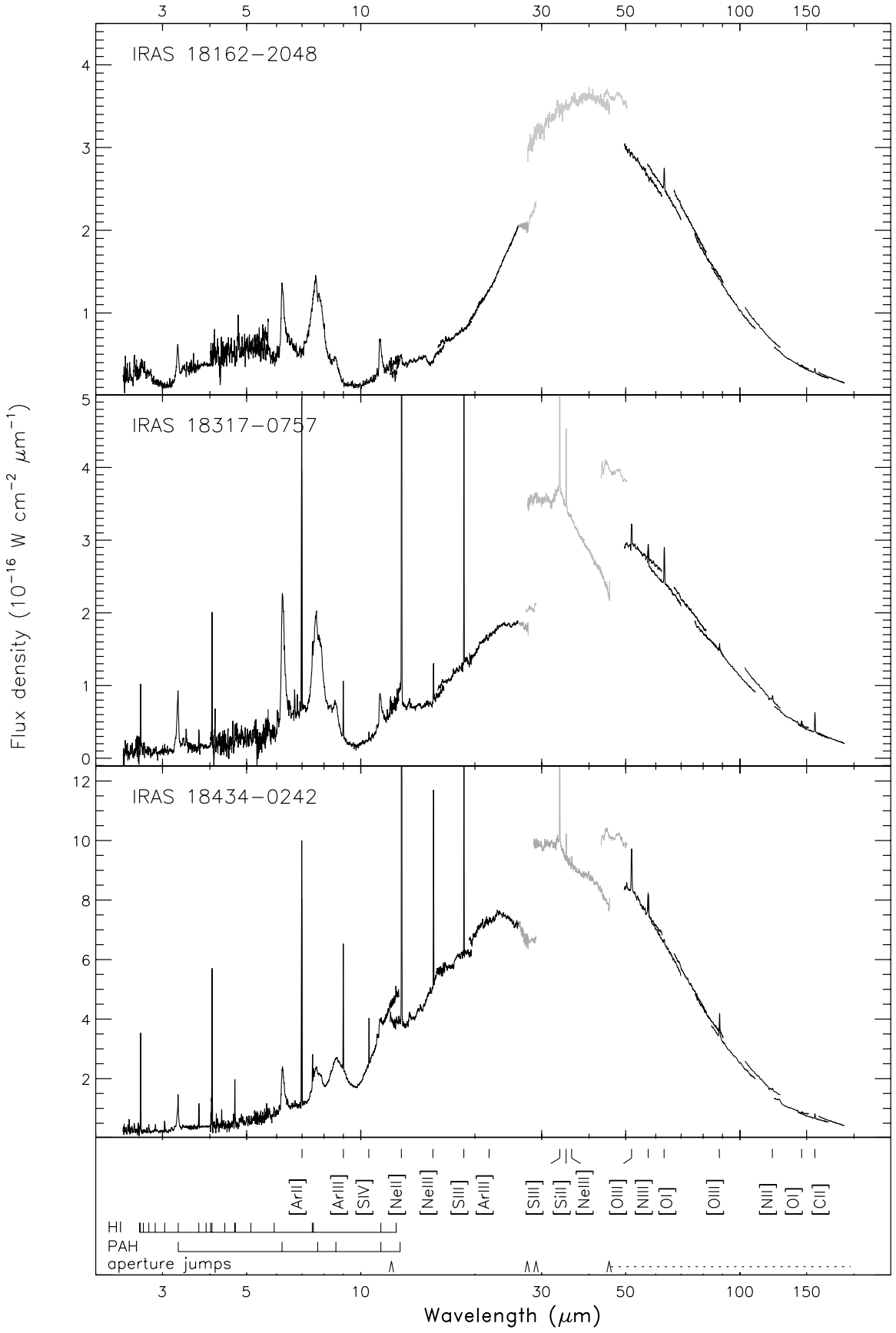

Fig. 8. continued.

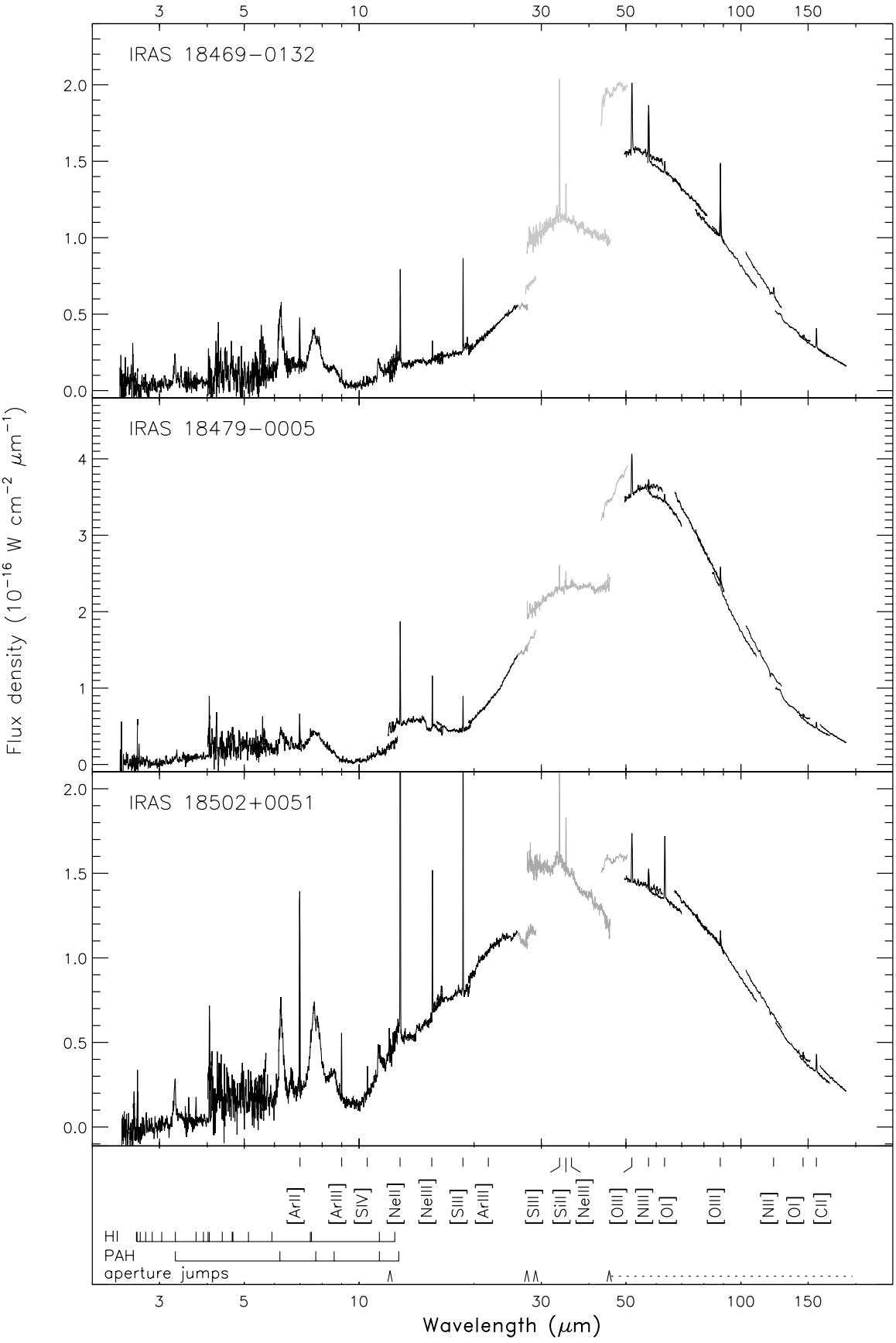

Fig. 8. continued.

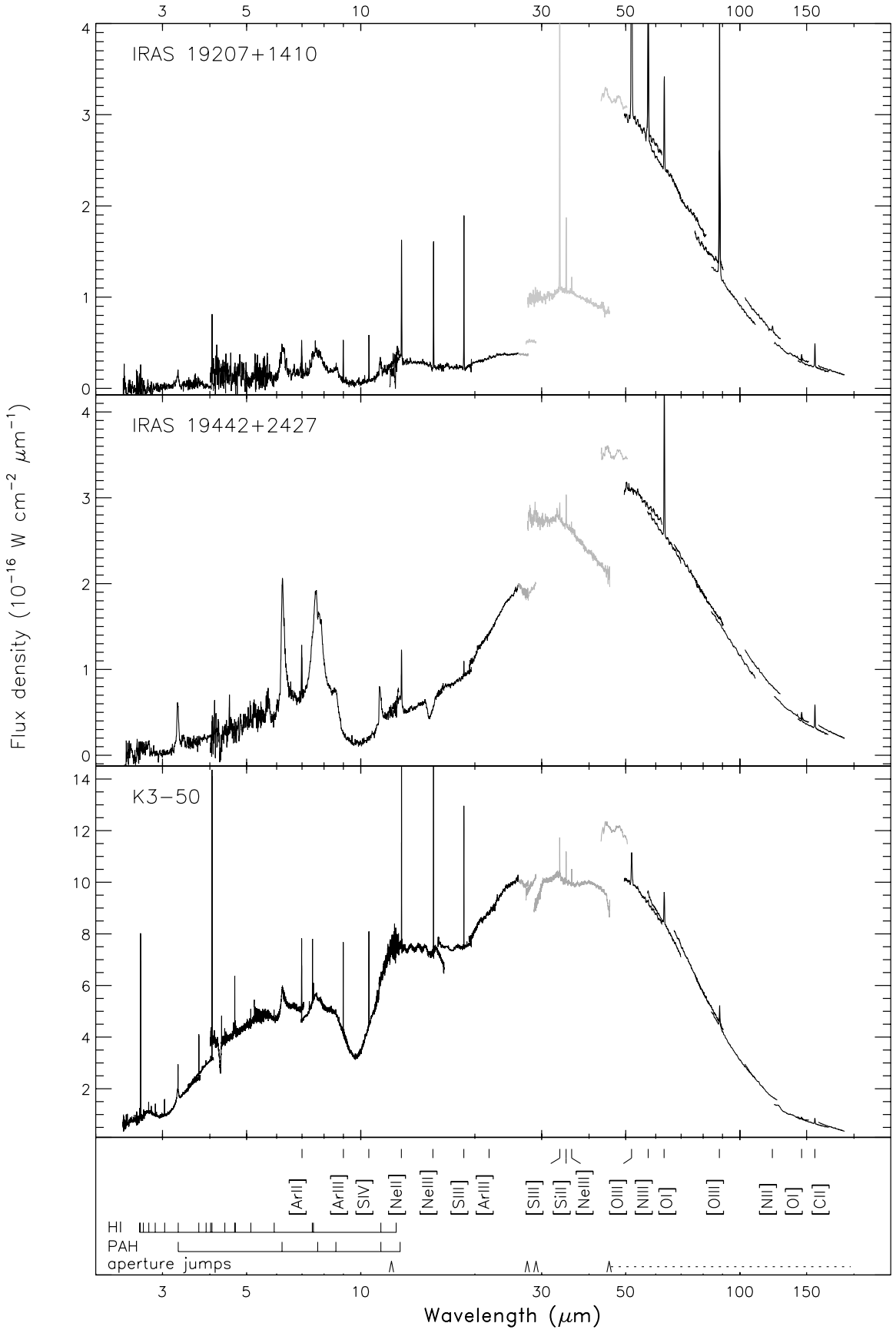

Fig. 8. continued.

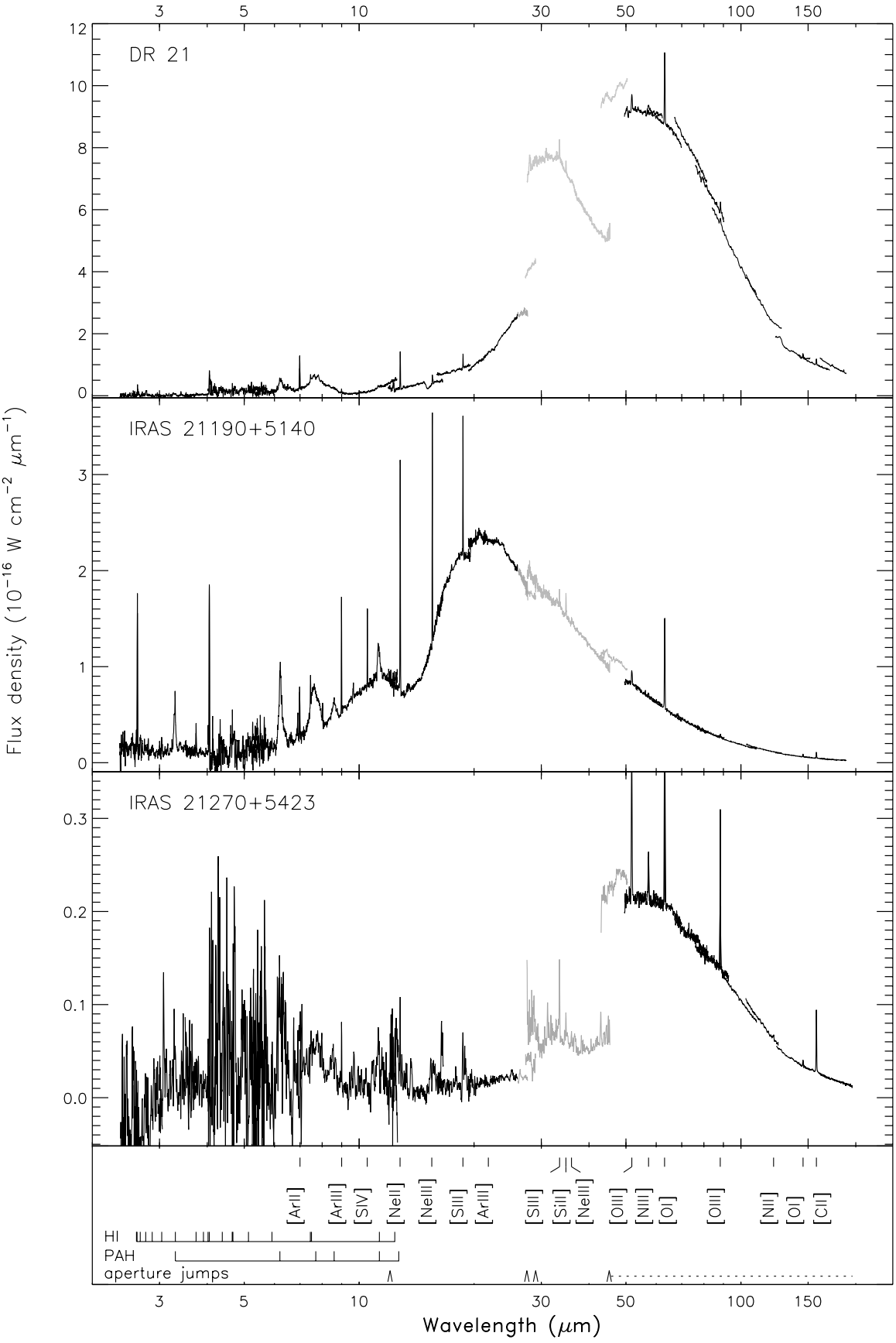

Fig. 8. continued.

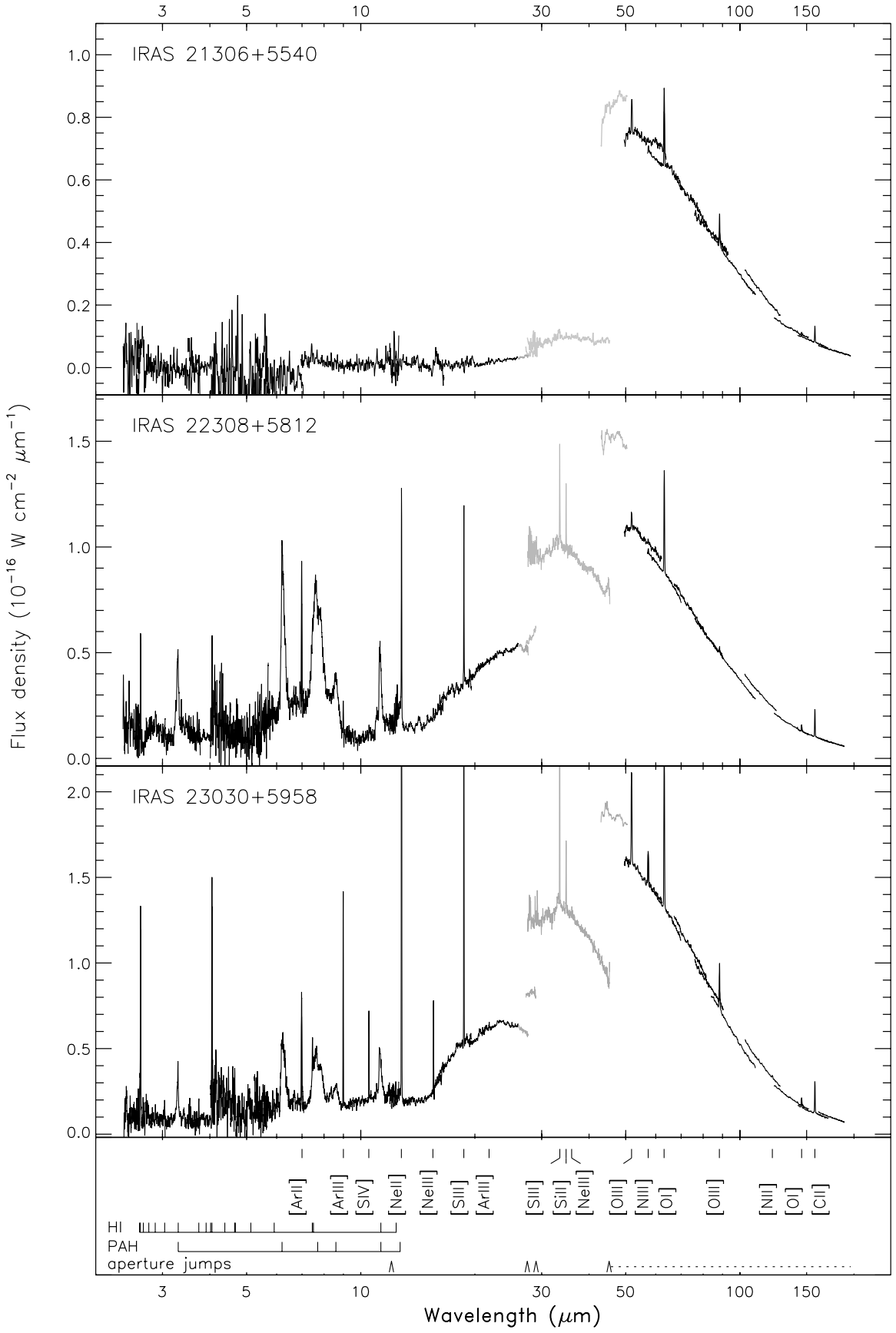

Fig. 8. continued.

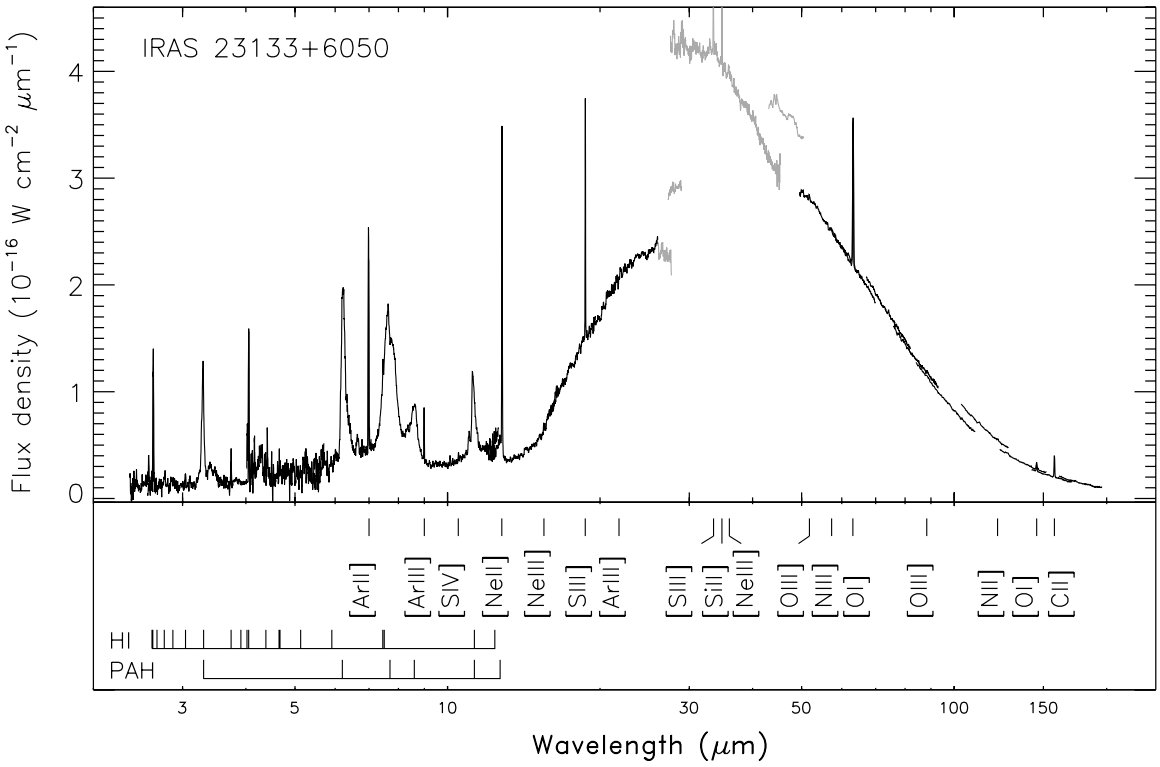

Fig. 8. continued.

band 3D and LWS SW1 detector are shown in grey tones. The spectral properties of each H II region are detailed in a series of tables which give the fluxes of the atomic fine-structure lines in the SWS (Table 5) and in the LWS (Table 6), the fluxes of the hydrogen recombination lines (Tables 7 and 8) and information on the presence of dust bands (Table 9) and molecular ices (Table 10).

The combined SWS–LWS spectra (Fig. 8) show that compact H II regions display a great diversity in their spectral properties. Generally, the infrared spectrum of an H II region is dominated by a strong dust continuum that peaks at $\sim$40 μm. On top of this continuum, there is a series of fine-structure lines and hydrogen recombination lines. In addition, a family of prominent dust bands (most notably the emission features present at mid-infrared wavelengths and attributed to small aromatic carbon species such as Polycyclic Aromatic Hydrocarbons or PAHs; Allamandola et al. 1989) and in some cases bands from molecular ice species (CO_2, H_2O). Finally, in a few cases, molecular lines of H_2 and OH are detected.

Detailed discussions of the atomic fine-structure from the ionised gas and the photo-dissociation regions (PDRs) are left to later publications (Paper II; Morisset et al. 2001; Damour et al. in prep.).

First studies on the dust properties in compact H II regions have been given in a series of papers (Roelfsema et al. 1996; Cox & Roelfsema 1999; Peeters et al. 1999; Van Kerckhoven et al. 2000; Hony et al. 2001) and a complete study will be presented in Peeters et al. (in prep.). The study of the dust continuum will be presented by Jones et al. (in prep.). The ice content in compact H II regions is discussed in Boogert (1999), Boogert et al. (in prep.). Hereafter we briefly describe the content of the infrared spectra of compact H II regions and outline the potential use of the present catalogue in future studies.

7.1. Atomic emission lines

In the spectra presented in Fig. 8, the main atoms (O, N, Ne, Ar, S, C and Si) are detected via their fine-structure lines. The lines of [C II], [O I] and [Si II], which originate in the PDRs associated with the H II regions, are seen in almost every source. They provide an important diagnostic of the physical conditions of the dense warm gas located just outside the ionised nebula. A detailed analysis will be given in Damour et al. (in prep.) where the present data will be compared to PDR model predictions. The strongest lines in the combined SWS–LWS spectra are emitted by atoms in the ionised nebula which, in rough order of importance, are the fine-structure lines of O^{++}, S^{++} and S^{+++}, Ne^{+} and Ne^{++}, Ar^{+} and Ar^{++} and N^{++} and N^{+} (see Fig. 8 and Tables 5 and 6). Except for oxygen, the species are present in different stages of ionisation and the range of ionisation potential sampled by these lines extends to $\sim$41 eV. This information allows us to describe the ionisation state of each H II region and to derive the properties of the exciting star(s). The H II regions studied in this paper form a prime sample to examine the variations of the nebular properties with galactocentric distance and to investigate the distribution of the relative and absolute element abundances in the Milky Way. The study of the ionisation state and the element abundance

based on the present sample of compact H II regions is the major aim of the UCH II ISO program and the subject of an accompanying paper (Martín-Hernández et al. 2002, i.e. Paper II).

In addition to the fine-structure lines, H I recombination lines are present in the spectra (see Fig. 8). These H I recombination lines are used to derive the extinction law at these wavelengths by comparing the observed line strengths to the predictions of recombination theory (see Paper II).

Some sources exhibit unusual lines. IRAS 12073 has an emission line at 4.3 μm ([KIV]?), IRAS 12331 at 21.8 and 27.1 μm (HI or [ArIII]; [SV]) and K3-50 A at 4.295, 4.377 and 4.617 (?, HI, [KIII]?). The SWS AOT06 of IRAS 18434 shows also the 4.617 μm [KIII] line.

7.2. Molecular emission lines

In a few sources, molecular lines of H_2 are detected. In one case, IRAS 21190+5140 (M1-78), six emission lines of molecular hydrogen are present in the SWS spectrum, i.e. 1–0 O(3) to O(5) and 0–0 S(3) to S(5). IRAS 12063 shows the 0–0 S(5) H_2 line and K3-50 A exhibits the 1–0 O(3) and 0–0 S(1) H_2 lines.

The molecular absorption line of OH at 119.2 μm is present in the following sources: IRAS 17221, IRAS 17279, IRAS 17455, IRAS 17591, IRAS 18032, IRAS 18317, IRAS 18434, IRAS 18469, IRAS 18479, IRAS 18502 and Sgr C. The latter sources also shows an OH absorption line at 79.3 μm. W3 A, IRAS 19442 and DR 21 exhibit CO emission lines (162.9, 173.6 and 185.9 μm). The H_2O emission line at 179.7 μm is clearly present in Sgr C.

7.3. Dust content

The infrared spectra of compact H II regions are dominated by a strong continuum due to the thermal emission of dust. As mentioned in Sect. 6.3, it is not straightforward to compare the obtained spectrum of an extended source over different aperture sizes. So, caution should be taken when studying the SED of a specific source when this source is not a point source. For most of the sources, this dust continuum seems to peak in the range 40–60 μm when plotted in μm versus W/cm^2/μm corresponding to dust temperatures of ∼60–70 K. In some cases (IRAS 11143, IRAS 12073, IRAS 21190 and perhaps IRAS 17455), the spectrum peaks at shorter wavelengths ∼30 μm, indicating that warmer dust is present in these nebulae. The H II regions in this sample appear to be substantially hotter than UC H II regions, with dust temperatures of ∼50 K. Probably, the nebulae in this sample are somewhat more evolved and emerging from their dust envelopes. In the case of IRAS 02575, a strong continuum is present shortwards of 5 μm, indicating temperatures in excess of ∼800 K. This unusual temperature for an H II region can be explained by the fact that, for this source, the SWS aperture encloses both the compact H II region and an Herbig AeBe star (see Sect. 6.2). Finally, many H II regions show continuum emission at $\lambda < 12$ μm, indicative of a high colour temperature. Yet, it cannot be due to small molecules (∼50 C-atoms) since those would give rise only to a weak quasi-continuum in this wavelength region (Allamandola et al. 1989). This continuum could be due to a small fraction of dust in the H II region heated to high temperatures by resonantly scattered Lyman-alpha radiation. The complete wavelength coverage from 2.3 to 196 μm provides in principle important information on the dust spectrum at mid-infrared wavelengths dominated by the PAH emission bands and the far-infrared continuum which is dominated by the bigger dust grains. Improvement in the SWS calibration will be crucial to further study this part of the spectrum.

The IR emission features at 3.3, 6.2, "7.7", 8.6 and 11.2 μm – commonly attributed to PAHs – are present in most of the spectra of the H II regions together with many weaker features e.g. the 12.7 μm band (see Table 9). The shape and strength of these dust bands exhibit considerable variations from source to source. At the spectral resolution of the present data, the bands are found to form complex emission patterns with a variety of subpeaks and spectral detail. For instance, the "7.7" μm band consists of two bands peaking at 7.6 and 7.8 μm. The variations in the relative intensities of the bands are thought to be primarily due to variations in the physical conditions of the emitting region (radiation field, density, etc.) that determines the physical (ionisation) and/or chemical processing of the interstellar PAH family (e.g. Roelfsema et al. 1996; Cox & Roelfsema 1999; Peeters et al. 1999). A complete analysis of the near- and mid-infrared dust bands in the spectra of compact H II regions, together with a study of the variation of their shapes and relative intensities as a function of the ionisation state (as measured by the atomic lines), will be presented in Peeters et al. (in prep.). In addition to these emission bands, a large number of the H II regions show in their infrared spectra the broad absorption band at 9.7 μm due to the stretching mode of amorphous silicate. The corresponding bending mode at 18 μm might be present in the spectra of some sources but is not always clearly visible. A summary of the dust content in the sample of H II regions of this catalogue is given in Table 9, where the presence of the dust emission bands and of the silicate absorption bands is indicated for each source. Sources which are not included in Table 9 do not show any emission/absorption features. Given the low continuum of some sources, it is not possible to assess the presence of absorption.

7.4. Ice content

Since compact H II regions are embedded sources, they are potential targets for absorption studies of molecular ices. As mentioned earlier, for two of the sources which were originally included in the sample, the combined SWS–LWS spectra were found to be dominated by absorption,

Table 5. The fluxes of the SWS fine-structure lines.

Source	Line fluxes[a,b] (10^{-18} W/cm^2)								
	[Ar II] 7.0 μm 8%[c]	[Ar III] 9.0 μm 8%[c]	[S IV] 10.5 μm 8%[c]	[Ne II] 12.8 μm 16%[c]	[Ne III] 15.5 μm 16%[c]	[S III] 18.7 μm 16%[c]	[S III] 33.5 μm 25%[c]	[Si II] 34.8 μm 25%[c]	[Ne III] 36.0 μm 25%[c]
IR 01045	<0.2	<0.1	<0.2	1.0 ± 0.2	0.6 ± 0.1	0.5 ± 0.2	<0.3	<0.3	<0.3
IR 01420	<0.2	<0.1	<0.2	<0.2	<0.2	<0.1	<0.3	<0.3	<0.3
IR 02219*	2.5 ± 0.2	12.5 ± 0.5	26 ± 1	36 ± 2	94 ± 2	59 ± 2	64 ± 5	18 ± 1	22 ± 2
IR 02219$^\diamond$	2.6 ± 0.1	13.7 ± 0.3	28 ± 1	39 ± 2	97 ± 3	43 ± 1	54 ± 5	15.1 ± 0.8	21 ± 5
IR 02383$^\natural$	<0.1	<0.1	<0.1	<0.2	<0.2	<0.2	<0.2	<0.2	<0.2
IR 02575	<0.1	<0.1	<0.1	<0.2	<0.2	<0.1	<0.3	0.5 ± 0.2	<0.3
IR 04025	<0.1	<0.1	<0.1	<0.1	<0.1	<0.1	<0.1	<0.1	<0.1
IR 05167	<0.2	<0.1	<0.1	<0.2	<0.1	<0.1	<0.1	<0.1	<0.1
IR 05221	<0.2	<0.1	<0.1	<0.1	<0.1	<0.1	<0.2	<0.2	<0.2
IR 06158$^\natural$	<0.2	<0.2	<0.2	<0.2	<0.2	<0.2	<0.3	1.3 ± 0.3	<0.4
IR 10589	3.1 ± 0.1	2.5 ± 0.1	1.5 ± 0.2	14 ± 1	4.1 ± 0.2	15.7 ± 0.4	14.8 ± 0.8	4.8 ± 0.5	<0.5
IR 11143	<0.1	1.38 ± 0.07	8.4 ± 0.3	2.5 ± 0.2	11.4 ± 0.5	7.8 ± 0.2	19 ± 1	1.4 ± 0.3	2.26 ± 0.10
IR 12063	0.99 ± 0.09	4.0 ± 0.2	9.1 ± 0.3	9.3 ± 0.6	18.9 ± 0.5	11.8 ± 0.2	10.5 ± 0.3	4.5 ± 0.7	2.8 ± 0.2
IR 12073	0.9 ± 0.3	11.9 ± 0.4	59 ± 2	14 ± 1	91 ± 7	35 ± 1	33 ± 2	8.8 ± 0.8	16.8 ± 0.8
IR 12331$^\natural$	0.87 ± 0.08	1.6 ± 0.1	1.28 ± 0.06	6.3 ± 0.3	4.63 ± 0.09	9.3 ± 0.3	23.7 ± 0.7	2.8 ± 0.3	1.4 ± 0.1
IR 15384	8.2 ± 0.5	5.0 ± 0.6	2.6 ± 0.1	34 ± 2	10 ± 1	25.9 ± 0.6	28 ± 1	8 ± 1	2.3 ± 0.3
IR 15502	4.4 ± 0.4	0.9 ± 0.1	0.23 ± 0.03	12 ± 1	3.1 ± 0.4	4.9 ± 0.4	9.5 ± 0.2	4.1 ± 0.9	<1.7
IR 16128$^\natural$	2.39 ± 0.09	1.0 ± 0.2	0.82 ± 0.03	7.7 ± 0.3	4.5 ± 0.1	6.4 ± 0.3	22 ± 2	6.1 ± 0.2	1.5 ± 0.3
IR 17160$^\natural$	1.6 ± 0.1	0.18 ± 0.03	<0.1	4.4 ± 0.4	0.9 ± 0.2	2.7 ± 0.1	12.3 ± 0.7	5.1 ± 0.2	<0.3
IR 17221$^\natural$	3.1 ± 0.1	0.76 ± 0.10	0.13 ± 0.03	10.2 ± 0.4	0.42 ± 0.09	7.3 ± 0.2	18 ± 2	3.9 ± 0.8	<0.3
IR 17279	2.4 ± 0.1	0.21 ± 0.04	<0.1	5.8 ± 0.3	0.4 ± 0.2	3.17 ± 0.08	13 ± 1	5.1 ± 0.2	<0.3
Sgr C	2.8 ± 0.2	<0.1	<0.09	4.7 ± 0.3	<0.2	1.6 ± 0.1	11 ± 1	10.1 ± 0.2	<0.4
IR 17455	5.9 ± 0.2	3.4 ± 0.1	1.9 ± 0.2	21 ± 1	9.7 ± 0.3	23.2 ± 0.4	30 ± 3	5.0 ± 0.5	1.3 ± 0.2
IR 17591	<0.2	<0.1	<0.1	0.9 ± 0.1	2.3 ± 0.3	0.93 ± 0.07	3.9 ± 0.2	1.5 ± 0.2	0.9 ± 0.2
IR 18032	5.1 ± 0.4	0.61 ± 0.04	<0.1	11.8 ± 0.7	<0.3	6.9 ± 0.3	11.8 ± 0.8	5.9 ± 0.4	<0.3
IR 18116	7.5 ± 0.4	0.79 ± 0.06	<0.2	14 ± 1	1.1 ± 0.2	14.1 ± 0.5	28 ± 2	7.2 ± 0.4	<0.4
IR 18162	<0.2	<0.1	<0.1	<0.3	<0.1	<0.2	<0.9	<1.0	<1.1
IR 18317$^\natural$	10.9 ± 0.3	2.1 ± 0.1	0.33 ± 0.08	34 ± 1	2.4 ± 0.2	25.6 ± 0.4	27.6 ± 1.0	9.0 ± 0.5	<0.5
IR 18434	22 ± 2	11.0 ± 0.7	4.2 ± 0.4	99 ± 7	27 ± 1	46 ± 1	39 ± 3	7 ± 1	3 ± 1
IR 18469	1.0 ± 0.3	0.2 ± 0.1	<0.10	2.4 ± 0.1	0.55 ± 0.02	2.8 ± 0.1	8.4 ± 0.9	2.4 ± 0.3	<0.4
IR 18479	1.06 ± 0.10	<0.1	<0.1	5.6 ± 0.4	2.7 ± 0.3	2.0 ± 0.1	2 ± 1	1.7 ± 0.2	<0.6
IR 18502	2.8 ± 0.3	0.93 ± 0.06	0.49 ± 0.07	15.5 ± 0.7	3.6 ± 0.2	8.6 ± 0.2	8.1 ± 0.6	2.8 ± 0.4	<0.4
IR 19207	1.0 ± 0.1	1.1 ± 0.1	1.41 ± 0.07	5.0 ± 0.4	5.7 ± 0.1	7.4 ± 0.3	27 ± 1	6.4 ± 0.7	1.6 ± 0.3
IR 19442	1.3 ± 0.1	<0.1	<0.1	2.8 ± 0.2	<0.1	0.8 ± 0.1	1.9 ± 0.3	3.8 ± 0.6	<0.6
IR 19598	2.2 ± 0.1	2.8 ± 0.1	3.3 ± 0.1	11.6 ± 0.4	27.9 ± 0.5	7.6 ± 0.2	4.6 ± 0.8	4.5 ± 0.7	1.9 ± 0.3
DR 21	2.8 ± 0.3	0.29 ± 0.05	<0.1	5.1 ± 0.2	1.5 ± 0.6	2.2 ± 0.2	5 ± 1	4 ± 1	<1.5
IR 21190	1.2 ± 0.1	3.11 ± 0.07	2.09 ± 0.08	10.1 ± 0.5	10.0 ± 0.3	6.51 ± 0.10	1.71 ± 0.09	2.8 ± 0.7	<0.44
IR 21270$^\natural$	<0.2	<0.1	<0.1	0.4 ± 0.1	<0.1	0.6 ± 0.2	1.2 ± 0.4	0.5 ± 0.2	<0.2
IR 21306$^\natural$	<0.2	<0.1	<0.1	<0.1	<0.2	<0.1	<0.2	<0.2	<0.1
IR 22308*	1.9 ± 0.1	0.45 ± 0.04	<0.1	3.9 ± 0.2	<0.1	4.0 ± 0.8	4.3 ± 0.4	2.9 ± 0.2	<0.3
IR 22308†	1.9 ± 0.3	0.4 ± 0.1	<0.1	3.5 ± 0.3	<0.2	3.3 ± 0.2	3.6 ± 0.3	2.6 ± 0.1	<0.3
IR 23030	1.8 ± 0.2	3.1 ± 0.2	1.3 ± 0.1	14.7 ± 0.5	2.12 ± 0.09	16.3 ± 0.4	14 ± 2	4.0 ± 0.5	<0.3
IR 23133	5.6 ± 0.3	1.22 ± 0.04	0.20 ± 0.05	12.7 ± 0.5	<0.3	10.0 ± 0.2	4.6 ± 0.8	8.3 ± 0.4	<0.9

[a] The listed errors are the square root of the quadratic sum of the difference between the up and down scan measurements and the statistical error of the line fitting (see Sect. 4). Hence *no* calibration uncertainties are included! To obtain the final error, see Sect. 4.2. [b] Note that these lines are seen through different apertures (see Table 2). [c] 1σ Absolute flux accuracy at this wavelength (see Table 2). $^\natural$ Approximate offset between the source peak and the ISO pointing direction $\geq 10''$. This data should be used with caution (see Sects. 4.3 and 6.2).
$^\circ$ TDT = 64600609; $^\diamond$ TDT = 78800709; * TDT = 17701258; † TDT = 56101082; see Sect. 3.1.4.

displaying a very rich set of molecular ice bands (see Dartois et al. 1998, and references therein).

For three of the sources presented in this paper, broad absorption bands of amorphous H_2O ice are clearly

Table 6. The fluxes of the LWS fine-structure lines.

Source	Line fluxes[a,b,c] (10^{-18} W/cm^2)						
	[O III] 51.8 μm	[N III] 57.3 μm	[O I] 63.1 μm	[O III] 88.3 μm	[N II] 121.8 μm	[O I] 145.5 μm	[C II] 157.7 μm
IR 01420	<0.5	<0.3	4.04 ± 0.08	<0.2	<0.1	0.24 ± 0.02	3.1 ± 0.3
IR 02219	336 ± 13	37 ± 7	126 ± 2	69 ± 1	<3.5	13.8 ± 0.7	23.5 ± 0.7
IR 02383	<0.6	<0.4	3.1 ± 0.4	<0.2	<0.2	0.09 ± 0.03	2.7 ± 0.4
IR 02575	<1.2	<0.6	8.5 ± 0.3	<0.4	<0.3	0.87 ± 0.05	4.9 ± 0.4
IR 04025	<0.5	<0.4	1.3 ± 0.2	<0.2	<0.1	0.076 ± 0.01	1.1 ± 0.1
IR 05167	<0.5	<0.3	1.7 ± 0.1	<0.1	<0.1	0.06 ± 0.01	2.0 ± 0.2
IR 05221	<0.6	<0.4	1.53 ± 0.07	<0.1	<0.1	0.24 ± 0.04	1.42 ± 0.07
IR 05302	<0.4	<0.3	<0.1	<0.1	<0.1	0.06 ± 0.04	0.44 ± 0.02
IR 05335	<0.5	<0.4	0.22 ± 0.06	<0.1	<0.04	<0.05	0.21 ± 0.05
IR 06158	<0.9	<0.8	30 ± 2	<0.4	<0.3	1.1 ± 0.1	6.9 ± 0.6
IR 10589	19.2 ± 0.8	5.0 ± 0.3	17.9 ± 0.7	9.2 ± 0.3	1.17 ± 0.09	2.06 ± 0.03	14.3 ± 0.8
IR 11143	88 ± 4	17.6 ± 0.7	5.9 ± 0.2	67 ± 2	0.7 ± 0.1	0.38 ± 0.04	5.7 ± 0.4
IR 12063	43 ± 2	6.5 ± 0.5	27.0 ± 0.8	13.5 ± 0.2	<0.5	2.76 ± 0.08	9.6 ± 0.6
IR 12073	408 ± 20	50 ± 2	121 ± 3	153 ± 1	<1.1	5.9 ± 0.2	24.3 ± 0.8
IR 12331	73 ± 2	23 ± 1	11.4 ± 0.4	35.8 ± 0.5	2.7 ± 0.1	2.29 ± 0.08	9.8 ± 0.5
IR 15384	68 ± 3	24.2 ± 0.8	56 ± 1	22.1 ± 0.4	3.9 ± 0.2	7.2 ± 0.2	25 ± 1
IR 15502	34 ± 3	19 ± 1	20 ± 3	20.5 ± 0.5	4.3 ± 0.1	4.1 ± 0.2	13.7 ± 0.5
IR 16128	129 ± 6	47 ± 1	39.0 ± 0.7	51.2 ± 0.6	5.3 ± 0.2	4.4 ± 0.3	19.4 ± 0.7
IR 17160	25.6 ± 0.8	15.0 ± 0.5	22.8 ± 0.6	14.8 ± 0.4	4.8 ± 0.5	3.3 ± 0.3	16.3 ± 0.6
IR 17221	13.7 ± 0.7	10.6 ± 0.5	8.8 ± 0.3	6.9 ± 0.2	6.0 ± 0.3	3.8 ± 0.2	11.4 ± 0.5
IR 17279	11.7 ± 0.6	13.4 ± 0.7	2.6 ± 0.2	13.0 ± 0.2	8.3 ± 0.4	1.66 ± 0.07	10.6 ± 0.7
Sgr C	8.6 ± 0.7	10.3 ± 0.3	14.8 ± 0.4	10.1 ± 0.6	15.8 ± 0.6	1.6 ± 0.2	31.6 ± 0.8
IR 17455	58 ± 4	28.8 ± 0.9	10.1 ± 0.3	30.9 ± 0.4	4.7 ± 0.2	2.3 ± 0.1	12.8 ± 0.4
IR 17591	29 ± 1	4.0 ± 0.3	6.2 ± 0.2	17.1 ± 0.3	1.10 ± 0.04	1.7 ± 0.2	9.3 ± 0.6
IR 18032	6.4 ± 0.9	4.5 ± 0.4	11.4 ± 0.5	3.5 ± 0.4	2.3 ± 0.4	2.8 ± 0.4	9.5 ± 0.3
IR 18116	16.0 ± 0.6	8.1 ± 0.7	57 ± 1	7.0 ± 0.2	3.1 ± 0.2	4.9 ± 0.1	19.0 ± 1.0
IR 18162	<1.5	<1.6	8.6 ± 0.2	<0.8	<0.5	1.37 ± 0.10	3.8 ± 0.3
IR 18317	9.7 ± 1.0	6.3 ± 0.4	16.0 ± 0.4	2.7 ± 0.2	4.7 ± 0.3	4.1 ± 0.2	18.4 ± 1.0
IR 18434	46 ± 2	22 ± 1	4.4 ± 0.4	19.4 ± 0.4	4.6 ± 0.2	3.2 ± 0.2	10.4 ± 0.7
IR 18469	14.1 ± 0.6	10.1 ± 0.5	2.34 ± 0.09	14.8 ± 0.2	3.6 ± 0.4	0.8 ± 0.1	8.6 ± 0.4
IR 18479	17.2 ± 0.8	2.5 ± 0.6	3.2 ± 0.3	7.0 ± 0.4	<1.1	2.4 ± 0.1	5.5 ± 0.2
IR 18502	8.7 ± 0.6	3.0 ± 0.4	12.1 ± 0.4	2.9 ± 0.1	<0.6	1.9 ± 0.2	7.1 ± 0.3
IR 19207	169 ± 9	47 ± 1	30.9 ± 0.6	96.7 ± 0.9	3.7 ± 0.2	4.0 ± 0.2	17.1 ± 0.9
IR 19442	<2.6	<1.7	54.7 ± 0.8	<1.0	<0.6	5.07 ± 0.08	17.9 ± 0.7
IR 19598	37 ± 1	4.6 ± 1.0	39.3 ± 0.9	21.5 ± 0.8	<1.1	4.4 ± 0.5	14.2 ± 0.9
DR 21	15 ± 1	<4.5	73 ± 1	11.4 ± 0.5	<2.3	9.9 ± 0.3	12.8 ± 0.2
IR 21190	4.5 ± 0.4	<1.0	30 ± 1	0.9 ± 0.1	<0.2	1.9 ± 0.2	4.0 ± 0.3
IR 21270	5.1 ± 0.2	1.4 ± 0.2	8.3 ± 0.2	4.89 ± 0.09	<0.3	0.43 ± 0.06	4.4 ± 0.7
IR 21306	3.4 ± 0.4	<0.7	5.4 ± 0.2	3.06 ± 0.09	<0.3	0.52 ± 0.06	3.4 ± 0.3
IR 22308*	2.4 ± 0.3	<0.6	15.8 ± 0.5	0.98 ± 0.08	<0.3	1.9 ± 0.1	8.1 ± 0.4
IR 22308†	2.4 ± 0.3	0.6 ± 0.2	15.4 ± 0.3	1.03 ± 0.09	<0.3	2.00 ± 0.04	8.6 ± 0.4
IR 23030	17.4 ± 0.8	5.6 ± 0.5	31.3 ± 0.4	7.3 ± 0.2	0.9 ± 0.1	3.23 ± 0.09	12 ± 1
IR 23133	1.4 ± 0.5	<1.1	43 ± 1	<0.8	0.8 ± 0.3	4.06 ± 0.09	12.9 ± 0.7

[a] The listed errors are the square root of the quadratic sum of the difference between the up and down scan measurements and the statistical error of the line fitting (see Sect. 4). Hence, *no* calibration uncertainties are included! To obtain the final error, see Sect. 4.2. [b] At these wavelengths the calibration uncertainty is 10%. [c] Note that these lines are seen through different apertures.
* TDT = 17701257; † TDT = 56101081; see Sect. 3.1.4.

detected at 3 and 6 μm (the stretching and bending modes, respectively). These bands might be present in some other sources but the low flux density levels (<5 Jy) in the 3 μm wavelength region results in noisy spectra from which firm conclusions cannot be drawn. In addition, the strong 3.3 and 6.2 μm dust emission bands are located in the red wing of both H_2O bands resp. making the situation difficult for sources with moderate amounts of extinction.

At longer wavelengths, the continuum becomes stronger making the situation more favourable to detect

Table 7. The fluxes of the H I recombination lines.

Source	Line fluxes[a,b] (10^{-18} W/cm^2)											
	HI (6–4) 2.625 μm 4%[c]	HI (13–5) 2.675 μm 4%[c]	HI (12–5) 2.757 μm 4%[c]	HI (11–5) 2.872 μm 4%[c]	HI (10–5) 3.038 μm 4%[c]	HI (9–5) 3.296 μm 4%[c]	HI (8–5) 3.739 μm 4%[c]	HI (5–4) 4.051 μm 4%[c]	HI (7–5) 4.652 μm 8%[c]	HI (6–5) 7.458 μm 8%[c]	HI (8–6) 7.500 μm 8%[c]	HI (9–7) 11.309 μm 8%[c]
IR 01045								0.2 ± 0.1				
IR 02219*	2.23 ± 0.09			0.25 ± 0.02	0.29 ± 0.08	0.6 ± 0.1	0.87 ± 0.04	6.6 ± 0.2	1.4 ± 0.2	3.0 ± 0.2		
IR 02219◇	2.2 ± 0.2		0.2 ± 0.1	0.20 ± 0.02	0.28 ± 0.03	0.41 ± 0.10	0.76 ± 0.07	6.7 ± 0.1	1.9 ± 0.2	3.1 ± 0.4	0.9 ± 0.4	
IR 02575								0.23 ± 0.02				
IR 10589	0.6 ± 0.1					0.10 ± 0.01		1.71 ± 0.04	0.34 ± 0.06	0.52 ± 0.07		
IR 11143	0.35 ± 0.05							0.68 ± 0.04		0.19 ± 0.07		
IR 12063	0.9 ± 0.2			0.10 ± 0.04	0.15 ± 0.03	0.23 ± 0.08	0.33 ± 0.04	2.08 ± 0.08		0.7 ± 0.2	0.29 ± 0.08	
IR 12073	2.8 ± 0.1	0.15 ± 0.05	0.16 ± 0.02	0.24 ± 0.04	0.36 ± 0.03	0.50 ± 0.04	0.86 ± 0.07	6.6 ± 0.3	1.7 ± 0.4	2.8 ± 0.2	0.8 ± 0.1	
IR 12331‡								0.51 ± 0.02				
IR 15384	1.0 ± 0.1			0.16 ± 0.06		0.21 ± 0.02	0.38 ± 0.05	2.86 ± 0.07	0.7 ± 0.2	0.85 ± 0.07		
IR 15502	0.32 ± 0.06					0.11 ± 0.05		1.5 ± 0.1		0.6 ± 0.2		
IR 16128‡	0.42 ± 0.04							0.63 ± 0.04		0.25 ± 0.03		
IR 17160‡								0.30 ± 0.02		0.3 ± 0.2		
IR 17221‡	0.19 ± 0.02							0.64 ± 0.07		0.43 ± 0.07		
IR 17279								0.30 ± 0.03				
Sgr C								0.23 ± 0.03				
IR 17455	0.59 ± 0.03					0.16 ± 0.03	0.32 ± 0.04	2.0 ± 0.1		0.7 ± 0.1		
IR 17591								0.15 ± 0.03		0.19 ± 0.04		
IR 18032						0.19 ± 0.03	0.15 ± 0.02	0.89 ± 0.07				
IR 18116	0.34 ± 0.03							0.93 ± 0.03				
IR 18317‡	0.56 ± 0.05					0.13 ± 0.01	0.22 ± 0.03	2.0 ± 0.1		0.81 ± 0.07	0.21 ± 0.04	
IR 18434	2.16 ± 0.05		0.26 ± 0.07	0.17 ± 0.07	0.35 ± 0.04	0.45 ± 0.02	0.88 ± 0.06	6.8 ± 0.3	1.9 ± 0.5	2.5 ± 0.2	0.75 ± 0.06	0.3 ± 0.1
IR 18469								0.25 ± 0.02				
IR 18479								0.57 ± 0.04				
IR 18502	0.23 ± 0.01							0.89 ± 0.04				
IR 19207								0.67 ± 0.05				
IR 19442								0.21 ± 0.09				
IR 19598	1.50 ± 0.08	0.05 ± 0.02	0.08 ± 0.02	0.125 ± 0.01	0.18 ± 0.02	0.28 ± 0.02	0.62 ± 0.03	4.7 ± 0.1	0.95 ± 0.08	1.96 ± 0.06	0.75 ± 0.07	
DR 21								0.88 ± 0.08		0.55 ± 0.03		
IR 21190	1.3 ± 0.1				0.13 ± 0.03	0.25 ± 0.02	0.27 ± 0.03	2.25 ± 0.08		0.76 ± 0.09		
IR 22308⋆	0.5 ± 0.1							0.62 ± 0.03				
IR 22308†								0.61 ± 0.03				
IR 23030	1.0 ± 0.2				0.12 ± 0.04	0.11 ± 0.05	0.15 ± 0.03	1.60 ± 0.06		0.6 ± 0.1	0.11 ± 0.04	
IR 23133	1.0 ± 0.1						0.31 ± 0.03	1.74 ± 0.10		0.5 ± 0.2		

[a] The listed errors are the square root of the quadratic sum of the difference between the up and down scan measurements and the statistical error of the line fitting (see Sect. 4) Hence *no* calibration uncertainties are included! To obtain the final error, see Sect. 4.2. [b] Note that these lines are seen through different apertures (see Table 2). [c] 1σ absolute flux accuracy at this wavelength (see Table 2). ‡ Approximate offset between the source peak and the ISO pointing direction $\geq 10''$. This data should be used with caution (see Sects. 4.3 and 6.2). ° TDT = 64600609; ◇ TDT = 78800709; ⋆ TDT = 17701258; † TDT = 56101082; see Sect. 3.1.4.

Table 8. The fluxes of extra H I recombination lines in K3-50 A.

Transition	λ (μm)	1 σ [a] %	Line fluxes[b] (10^{-18} W/cm^2)
14–5	2.613	4	0.05 ± 0.01
16–6	3.812	4	0.03 ± 0.02
15–6	3.906	4	0.07 ± 0.01
14–6	4.020	4	0.09 ± 0.04
12–6	4.376	4	0.3 ± 0.2
11–6	4.673	8	0.12 ± 0.06
10–6	5.127	8	0.2 ± 0.1
9–6	5.907	8	0.24 ± 0.06
10–7	8.760	8	0.12 ± 0.01

[a] 1σ absolute flux accuracy (see Table 2). [b] The listed errors are the square root of the quadratic sum of the difference between the up and down scan measurements and the statistical error of the line fitting (see Sect. 4). Hence *no* calibration uncertainties are included! To obtain the final error, see Sect. 4.2.

ice bands in absorption. The CO_2 bending mode at 15 μm is detected in 6 sources (listed in Table 10). Small variations in the substructure of the absorption band show that the ices have only been partially thermally processed ($45 < T < 90$ K) by the central heating source, in contrast to some highly processed regions around hot cores such as Sh 140 (Gerakines et al. 1999). Furthermore, extensive laboratory studies of the band profile show that interstellar CO_2 must be mixed with H_2O and CH_3OH ices (see Boogert 1999; Boogert et al. in prep.). The intrinsically stronger CO_2 stretching mode (4.27 μm) is present in the spectra of 3 sources (Table 10), but the data are of much lower quality due to the lower level of the continuum at these wavelength. Furthermore, it is located in AOT Band 2A, which tends to be very noisy. It is thus not excluded that the CO_2 stretching mode could be present in other compact H II regions than those listed in Table 10.

Finally, K3-50A is the only source in the present sample that shows an absorption band around 6.85 μm (Table 10). The analysis of this band is difficult since it is located in a complex spectral region which includes the 6.0 μm H_2O ice absorption band, the 6.2 μm PAH emission feature, the 6.8 μm absorption feature and the emission plateau between the 6.2 and "7.7" μm PAH bands. The derived profile is similar in appearance to absorption features seen toward dense molecular clouds exhibiting signs of warmer ice (Keane et al. 2001).

8. Conclusions

The ISO spectral catalogue of compact H II regions presents grating spectra from 2.5 to 196 μm of 43 compact H II regions which were taken with the two spectrometers (the SWS and the LWS) on board ISO. The infrared spectra of compact H II regions show a great diversity both in the dust and ice content, the dust continuum, the hydrogen recombination lines and in the relative intensities of the atomic fine-structure lines. This set of data will be a useful source of information to study the properties of the ionised gas, the dust and the photodissociation regions associated with compact H II regions and to investigate their variations across the Galactic plane. The spectra and the line fluxes, which form the core of

Table 9. The dust and silicate features present in the sources. The central wavelength is given in μm.

Source	PAHs						Silicate[a]
	3.3	6.2	7.7	8.6	11.2	12.7	9.7
IR 01045*	??	√	√	√	√	-	-
IR 02219	√	√	√	√	√	?	√
IR 02575	√	√	√	√	√	√	√
IR 06158*	??	??	??	-	-	-	-
IR 10589	√	√	√	√	√	-	?
IR 12063	√	√	√	√	√	-	√
IR 12073	√	√	√	√	√	√	-
IR 12331	?	√	√	√	√	√	-
IR 15384	√	√	√	√	√	√	√
IR 15502	√	√	√	√	√	-	√
IR 16128	√	√	√	√	√	√	√
IR 17160	√	√	√	√	√	√	√
IR 17221	√	√	√	√	√	√	√
IR 17279	√	√	√	√	√	√	?
Sgr C	√	√	√	√	√	√	√
IR 17455	√	√	√	√	√	?	√
IR 17591	-	√	√	√	√	√	-
IR 18032	√	√	√	√	√	√	√
IR 18116	√	√	√	√	√	√	?
IR 18162	√	√	√	√	√	√	√
IR 18317	√	√	√	√	√	√	√
IR 18434	√	√	√	√	√	-	√
IR 18469	√	√	√	√	√	√	√
IR 18479	?	√	√	?	√	-	√
IR 18502	√	√	√	√	√	√	√
IR 19207	√	√	√	√	√	√	√
IR 19442	√	√	√	√	√	√	√
IR 19598	√	√	√	√	√	-	√
DR 21	-	√	√	√	√	-	√
IR 21190	√	√	√	√	√	√	√
IR 21270*	-	√	√	√	?	-	-
IR 22308	√	√	√	√	√	√	-
IR 23030	√	√	√	√	√	√	-
IR 23133	√	√	√	√	√	√	-

[a] Silicate absorption feature. * Very low flux spectra.

Table 10. The ice features present in the sources. The central wavelength is given in μm.

Source	H_2O Ices		CO_2 Ices		Ice ?
	3	6	4.27	15.2	6.85
IR 02575	√	√	√	√	-
IR 17160	-	-	-	?	-
IR 18162	√	√	√	√	-
IR 18479	-	-	?	√	-
IR 19442	-	?	?	√	-
IR 19598	√	√	√	√	√
DR 21	-	-	-	√	-

this paper, were derived using the latest knowledge available on the calibration of the ISO spectra. The spectra of this catalogue will be made public on the ISO web page (`http://www.iso.vilspa.esa.es/`) for general use. Based on this catalogue, an accompanying paper describes first results on the ionisation structure and element abundance gradient (Paper II, Martín-Hernández et al. 2002) while a second paper presents a detailed model for IRAS 18434−0242 (Morisset et al. 2001). Forthcoming papers will describe the physical properties of the associated PDRs (Damour et al. in prep.), the PAH characteristics (Peeters et al. in prep.) and the CO_2 absorption bands (Boogert et al. in prep.).

Acknowledgements. The authors wish to thank the anonymous referee for usefull comments. EP thanks especially J. Cami, R. Shipman, D. Kester, F. Lahuis, S. Hony, A. Boogert, L. Decin and B. Vandenbussche for the support concerning the SWS data reduction. NLMH acknowledges the support of S. Sidher for the LWS data reduction. IA^3 is a joint development of the SWS consortium. Contributing institutes are SRON, MPE, KUL and the ESA Astrophysics Division. The SWS work was supported by the Dutch ISO Data Analysis Centre (DIDAC) at the Space Research Organisation Netherlands (SRON) in Groningen, The Netherlands. The ISO Spectral Analysis Package (ISAP) is a joint development by the LWS and SWS Instrument Teams and Data Centers. Contributing institutes are CESR, IAS, IPAC, MPE, RAL and SRON. LIA is a joint development of the LWS consortium. Contributing institutes are CESR, DRAL, IPAC and the ESA Astrophysics Division. EP acknowledges the support from an NWO program subsidy (grant number 783-70-000). NLMH acknowledges the support from an Ubbo Emmius grant for graduate students at the Rijksuniversiteit Groningen.

References

Afflerbach, A., Churchwell, E., Acord, J. M., et al. 1996, ApJS, 106, 423
Afflerbach, A., Churchwell, E., & Werner, M. W. 1997, ApJ, 478, 190
Allamandola, L. J., Tielens, G. G. M., & Barker, J. R. 1989, ApJS, 71, 733
Anglada, G., Estalella, R., Pastor, J., et al. 1996, ApJ, 463, 205
Barsony, M. 1989, ApJ, 345, 268
Becker, R. H., White, R. L., Helfand, D. J., & Zoonematkermani, S. 1994, ApJS, 91, 347
Blitz, L., Fich, M., & Stark, A. A. 1982, ApJS, 49, 183
Boogert, A. C. A. 1999, Ph.D. Thesis
Brand, J., & Wouterloot, J. G. A. 1994, A&AS, 103, 503
Bronfman, L., Nyman, L., & May, J. 1996, A&AS, 115, 81
Carpenter, J. M., Snell, R. L., & Schloerb, F. P. 1990, ApJ, 362, 147
Caswell, J. L., & Haynes, R. F. 1987, A&A, 171, 261
Cesaroni, R., Churchwell, E., Hofner, P., et al. 1994, A&A, 288, 903
Chan, K., & Onaka, T. 2000, ApJ, 533, L33
Churchwell, E. 1990, A&AR, 2, 79
Clegg, P. E., Ade, P. A. R., Armand, C., et al. 1996, A&A, 315, L38
Colgan, S. W. J., Simpson, J. P., Rubin, R. H., et al. 1991, ApJ, 366, 172
Cox, P., & Roelfsema, P. 1999, in Solid Interstellar matter: the ISO Revolution, ed. L. d'Hendecourt, C. Joblin, & A. Jones (EDP Sciences), 151
Dartois, E., Cox, P., Roelfsema, P. R., et al. 1998, A&A, 338, L21
de Graauw, T., Haser, L. N., Beintema, D. A., et al. 1996, A&A, 315, L49
de Vries, C. P., Brand, J., Habing, H. J., et al. 1984, A&AS, 56, 333
Depree, C. G., Goss, W. M., Palmer, P., & Rubin, R. H. 1994, ApJ, 428, 670
Faison, M., Churchwell, E., Hofner, P., et al. 1998, ApJ, 500, 280
Feldt, M., Stecklum, B., Henning, T., et al. 1999, A&A, 346, 243
Fey, A. L., Gaume, R. A., Claussen, M. J., & Vrba, F. J. 1995, ApJ, 453, 308
Fich, M. 1986, AJ, 92, 787
Fich, M. 1993, ApJS, 86, 475
Fich, M., & Blitz, L. 1984, ApJ, 279, 125
Fouks, B. I., & Schubert, J. 1995, Proc. of SPIE, 2475, 487
Garay, G., & Lizano, S. 1999, PASP, 111, 1049
Garay, G., Lizano, S., & Gomez, Y. 1994, ApJ, 429, 268
Garay, G., Rodriguez, L. F., Moran, J. M., & Churchwell, E. 1993, ApJ, 418, 368
Gry, C., Swinyard, B., Harwood, A., et al. 2000, LWS handbook: `http://www.iso.vilspa.esa.es/users/expl_lib/LWS_top.html`
Herter, T., Helfer, H. L., Briotta, D. A., et al. 1982, ApJ, 262, 153
Herter, T., Helfer, H. L., Forrest, W. J., et al. 1981, ApJ, 250, 186
Ho, P. T. P., Haschick, A. D., & Israel, F. P. 1981, ApJ, 243, 526
Hony, S., Van Kerckhoven, C., Peeters, E., et al. 2001, A&A, 370, 1030
Isaacman, R. 1984, MNRAS, 208, 399
Keane, J. V., Tielens, A. G. G. M., Boogert, A. C. C., et al. 2001, A&A, 376, 254
Kessler, M. F., Steinz, J. A., Anderegg, M. E., et al. 1996, A&A, 315, L27
Kester, D. J. M. 2001, `http://sws.ster.kuleuven.ac.be/`
Kim, K., & Koo, B. 2001, ApJ, 549, 979
Kurtz, S., Churchwell, E., & Wood, D. O. S. 1994, ApJS, 91, 659
Kurtz, S. E., Watson, A. M., Hofner, P., & Otte, B. 1999, ApJ, 514, 232
Leech, K., the SWS Instrument Dedicated Team and the SWS Instrument Support Team, 2001, SWS handbook: `http://www.iso.vilspa.esa.es/users/expl_lib/SWS_top.html`
Lis, D. C. 1991, ApJL, 379, L53
Liszt, H. S. 1992, ApJS, 82, 495
Liszt, H. S., & Spiker, R. W. 1995, ApJS, 98, 259
Martín-Hernández, N. L., Peeters, E., Morisset, C., et al. 2002, A&A, 381, 606 (Paper II)
McCutcheon, W. H., Sato, T., Dewdney, P. E., & Purton, C. R. 1991, AJ, 101, 1435
Megeath, S. T., Herter, T., Gull, G. E., & Houck, J. R. 1990, ApJ, 356, 534
Mehringer, D. M. 1994, ApJS, 91, 713

Mehringer, D. M., Goss, W. M., Lis, D. C., et al. 1998, ApJ, 493, 274
Morisset, C., Schaerer, D., Martín-Hernández, N. L., et al. 2001, A&A, submitted
Peeters, E., Tielens, A. G. G. M., Roelfsema, P. R., & Cox, P. 1999, ESA SP-427: The Universe as Seen by ISO, 427, 739
Plume, R., Jaffe, D. T., & Evans, N. J. 1992, ApJS, 78, 505
Reifenstein, E. C., Wilson, T. L., Burke, B. F., et al. 1970, A&A, 4, 357
Roelfsema, P. R., Cox, P., Tielens, A. G. G. M., et al. 1996, A&A, 315, L289
Roelfsema, P. R., & Goss, W. M. 1991, A&AS, 87, 177
Roelfsema, P. R., Goss, W. M., & Geballe, T. R. 1988, A&A, 207, 132
Roelfsema, P. R., Goss, W. M., & Geballe, T. R. 1989, A&A, 222, 247
Rudolph, A. L., Brand, J., de Geus, E. J., & Wouterloot, J. G. A. 1996, ApJ, 458, 653
Rudolph, A. L., Simpson, J. P., Haas, M. R., et al. 1997, ApJ, 489, 94
Salama, A. 2000, in ISO Beyond Point Sources: Studies of Extended IR Emission, ESA-SP-455
Shepherd, D. S., & Churchwell, E. 1996, ApJ, 457, 267
Shipman, R., & Lahuis, F. 2000, `http://sws.ster.kuleuven.ac.be/`
Simpson, J. P., Colgan, S. W. J., Rubin, R. H., et al. 1995, ApJ, 444, 721
Simpson, J. P., & Rubin, R. H. 1990, ApJ, 354, 165
Swinyard, B. M., Burgdorf, M. J., Clegg, P. E., et al. 1998, Proc. of SPIE, 3354, 888
Takahashi, H., Matsuhara, H., Watarai, H., & Matsumoto, T. 2000, ApJ, 541, 779
Tieftrunk, A. R., Gaume, R. A., Claussen, M. J., et al. 1997, A&A, 318, 931
Valentijn, E. A., Feuchtgruber, H., Kester, D. J. M., et al. 1996, A&A, 315, L60
Van Kerckhoven, C., Hony, S., Peeters, E., et al. 2000, A&A, 357, 1013
Walmsley, C. M., Churchwell, E., & Terzian, Y. 1981, A&A, 96, 278
Watarai, H., Matsuhara, H., Takahashi, H., & Matsumoto, T. 1998, ApJ, 507, 263
Wood, D. O. S., & Churchwell, E. 1989, ApJS, 69, 831
Wouterloot, J. G. A., & Brand, J. 1989, A&AS, 80, 149